Journal of Wind Engineering & Industrial Aerodynamics 199 (2020) 104132

Contents lists available at ScienceDirect

Journal of Wind Engineering & Industrial Aerodynamics

journal homepage: www.elsevier.com/locate/jweia

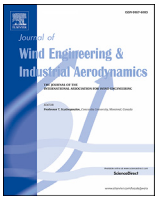

Reducing wind-induced vibrations of road sign structures through aerodynamic modifications: A computational pilot study for a practical example

Qiming Zhu [a], Stein K.F. Stoter [a], Michael Heisel [a,b], Catherine E. French [a], Michele Guala [a,b], Lauren E. Linderman [a], Dominik Schillinger [a,*]

[a] Department of Civil, Environmental, and Geo-Engineering, University of Minnesota, Twin Cities, MN, USA
[b] Saint Anthony Falls Laboratory, University of Minnesota, Twin Cities, MN, USA

ARTICLE INFO

Keywords:
Road sign structures
Wind-induced vibrations
Aerodynamic modifications
Finite element method
CFD validation

ABSTRACT

In this article, we illustrate the potential of aerodynamic modifications of road signs to reduce wind-induced vibrations. Using a real-world sign structure operated by the Minnesota Department of Transportation, we focus on two modification variants, one based on the simple removal of secondary panels and one based on the addition of drag reducing rear extensions to the main panel. Our main analysis tool is a computational fluid dynamics framework based on the finite element method, which is validated against experiments with a scaled sign model that were conducted in the towing tank and the wind tunnel of the St. Anthony Falls Laboratory. We demonstrate computationally that aerodynamic modifications constitute an effective way of reducing the vibration amplitude in the example structure for head wind at the average operating wind speed. The present study can be seen as a first step towards establishing the use of aerodynamic devices for road sign structures.

1. Introduction

Roadway signs and signals are lightweight structures that are deployed at the side of or above roads to give instructions or provide information to drivers. In most countries, roadside structures within a specified distance of the roadway must feature breakaway mechanisms to reduce injury of vehicle drivers and passengers in the case of impact, see e.g. the AASHTO 2015 LRFD specifications (American Association of State Highway and Transportation Officials, 2015) in the United States. Breakaway mechanisms often prohibit the stiffening of support structures, thus reducing the critical eigenfrequency such that signs become increasingly susceptible to wind-induced vibrations. Vibrations may lead to fatigue and potentially result in the premature failure of the support structure (Constantinescu et al., 2018; Finley, 2018). In addition, visible vibrations, even when not detrimental, may impact the serviceability of the sign and deflect the attention of passing vehicle drivers. Therefore, minimizing wind-induced vibrations constitutes a key concern in the design of road signs.

In this article, we present a computational pilot study that illustrates the potential of aerodynamic modifications to effectively alleviate wind-induced vibrations of road signs without stiffening the support structure. In particular, we focus on the case of head wind. Its direction corresponds both to the direction of weakest sign stiffness and to the direction of a potential approaching vehicle, so that adding stiffness for head wind loading is likely to conflict with breakaway mechanisms. We demonstrate the potential of aerodynamic modifications for a representative example, the rural intersection conflict warning sign (RICWS) operated by the Minnesota Department of Transportation. Due to its non-standard configuration, we resort to computational fluid dynamics (CFD) that has been successfully applied for accurately calculating transient spatially varying pressure distributions on complex sign configurations due to wind loading (Constantinescu et al., 2007; Beneberu et al., 2014) or passing vehicles (Lottes et al., 2011).

In a first step, we set up a CFD model of the RICWS and validate it against towing tank and wind tunnel experiments with a scaled physical model, carried out at the St. Anthony Falls Laboratory. In a second step, we use the validated CFD model at the field scale to determine transient pressure data on the original RICWS. Using one-way coupling (Constantinescu et al., 2007; Beneberu et al., 2014; Lottes et al., 2011), the pressure data is then transferred as the loading input to an Abaqus finite

---

* Corresponding author. Department of Civil, Environmental, and Geo- Engineering, University of Minnesota, 500 Pillsbury Drive S.E., Minneapolis, MN, 55455, USA.

E-mail address: dominik@umn.edu (D. Schillinger).

https://doi.org/10.1016/j.jweia.2020.104132
Received 2 May 2019; Received in revised form 20 February 2020; Accepted 20 February 2020
Available online 9 March 2020
0167-6105/© 2020 Elsevier Ltd. All rights reserved.

element model that simulates the structural dynamics response. We note that one-way coupling does not account for the impact of aeroelastic effects on the vibration response. Taking into account aeroelastic effects such as aerodynamic damping and aerodynamic stiffness that arise from the interaction of the structural motion with the air flow would require a fully nonlinear two-way coupling of our CFD and Abaqus models (Païdoussis et al., 2010; Bazilevs et al., 2013).

We then use our computational framework to explore the effectiveness of two possible modifications of the original RICWS configuration, with the goal of reducing its drag coefficient and vibration amplitude under moderate head wind. We first remove (possibly dispensable) panels positioned at the top of the original RICWS structure, a modification that stays in the realm of standard sign configurations. We then add short aerodynamic extensions to the main RICWS panel, resulting in a modified sign configuration that goes beyond what is current practice in the design of road signs. The idea is motivated by the recent success of using rear extensions in reducing drag for trailer trucks (Storms et al., 2004; Browand et al., 2005; McCallen et al., 2005; Håkansson and Lenngren, 2010; Hyams et al., 2011). We asses the ability of each configuration to improve the aerodynamic properties of the original RICWS, including the reduction of the drag, the turbulent kinetic energy in the wake of the sign and the amplitude of the vibrations of the structure.

The article is structured as follows: in Section 2, we provide a summary of the computational methods for fluid dynamics modeling used in this study. In Section 3, we describe the RICWS and its transfer into a CFD model, and discuss the validation against experiments at the laboratory scale. Section 4 focuses on the two aerodynamic modifications of the RICWS and assess the resulting aerodynamic and structural properties with respect to the original configuration. In Section 5, we summarize our results, draw conclusions, and motivate avenues for future work.

2. A finite element framework for computational fluid dynamics

Since the 1970's, computational fluid dynamics (CFD) techniques based on the numerical solution of the Navier-Stokes equations (or simplifications thereof) have been established to find shapes with minimal aerodynamic drag by means of computer simulations, see e.g. (Oberkampf et al., 2004; Cummings et al., 2015; Witherden and Jameson, 2017). In this section, we briefly describe the major components of our computational fluid dynamics framework, that consists of the finite element method, the variational multiscale method for stabilization and turbulence modeling, and special inflow boundary conditions for modeling incoming turbulence.

2.1. Finite element discretization of the incompressible Navier-Stokes equations

Many aerodynamic flow situations, including the current case of flow around a road sign, can be modeled by the incompressible Navier-Stokes equations:

$$\frac{\partial \mathbf{u}}{\partial t} + \nabla \cdot (\mathbf{u} \otimes \mathbf{u}) = \nabla \cdot (2\nu \nabla^s \mathbf{u} - p\mathbf{I}) + \mathbf{f} \tag{1}$$

$$\nabla \cdot \mathbf{u} = 0 \tag{2}$$

where $\mathbf{u}(\mathbf{x}, t)$ is the velocity vector, $p(\mathbf{x}, t)$ is the density normalized pressure, $\mathbf{I}$ is the identity tensor, ν is the kinematic viscosity and $\mathbf{f}(\mathbf{x}, t)$ is the prescribed density normalized body force. Equation (1) represents balance of momentum in the three spatial directions and equation (2) represents mass conservation for incompressible fluids.

To computationally solve for the velocity and pressure fields, equations (1) and (2) need to be discretized. Our framework uses the finite element method in space (Hughes, 2000; Donea and Huerta, 2003; Zienkiewicz and Taylor, 2005), combined with a second order generalized-α finite difference scheme in time (Jansen et al., 2000). The finite element formulation can be summarized as follows: find the approximate solutions $\{\mathbf{u}_h, p_h\}$ in the discrete function space $\mathscr{V}_h$ such that for all functions $\{\mathbf{v}_h,\ q_h\}$ in $\mathscr{V}_h$:

$$\begin{aligned}\left(\mathbf{v}_h, \frac{\partial \mathbf{u}_h}{\partial t}\right) - (\nabla \mathbf{v}_h, \mathbf{u}_h \otimes \mathbf{u}_h) - (\nabla \cdot \mathbf{v}_h, p_h) + (\nabla^s \mathbf{v}_h, 2\nu \nabla^s \mathbf{u}_h)\\ + (q_h, \nabla \cdot \mathbf{u}_h) = (\mathbf{v}_h, \mathbf{f})\end{aligned} \tag{3}$$

The no-slip and zero pressure boundary conditions are incorporated directly in the space $\mathscr{V}_h$, which, in our case, is a standard $\mathscr{C}^0$ continuous vector finite element space that consists of piecewise linear polynomials defined on tetrahedral elements. The standard Newton-Raphson algorithm is applied to tackle the nonlinearity of (3) with respect to $\mathbf{u}_h$.

It is important to note that the finite element formulation 3 is not naturally stable. Following (Tezduyar, 1991; Bazilevs et al., 2007; Hughes and Sangalli, 2007; Hughes et al. 2018 Franca), stabilization can be achieved via the addition of a subgrid-scale model based on the variational multiscale method. The basic idea of the subgrid-scale model is to include the effect of flow scales that cannot be resolved by the current finite element mesh. In this sense, it also serves as a turbulence model, as described in more detail in the following subsection.

2.2. A subgrid-scale model based on the variational multiscale method

Any attempt at computing the complete range of scales in a turbulent flow at moderate to high Reynolds numbers would result in extremely fine meshes with a prohibitively large number of degrees of freedom. The dissipative effect of the fine-scale components, however, cannot simply be omitted, as it significantly influences the overall flow characteristics. Therefore, the simulation of turbulent flows requires a suitable turbulence model (Spalart, 2000; Sagaut, 2006; Menter).

In a finite element framework, the variational multiscale method offers a foundation for characterizing the nature of the scale interaction and for quantifying subgrid-scale effects (Bazilevs et al., 2007; Hughes, 1995; Hughes et al., 1998; Yan et al., 2017). It can be interpreted as a reformulation of the classical large eddy simulation (LES), where the filtering operation that explicitly separates resolved and unresolved scales is replaced by performing a decomposition of the function spaces associated with the weak formulation. For more details on the relation between the variational multiscale method and the standard LES approach, we refer the interested readers to (Hughes et al., 2000, 2005; Tran and Sahni, 2017) and the references therein.

In the current scope, we briefly illustrate the variational multiscale procedure for the following abstract problem:

$$\begin{aligned}&\text{Find}\ \ \mathbf{u} \in \mathscr{V}\ \ \text{s.t.}\ \ \forall\, \mathbf{v} \in \mathscr{V}:\\ &\quad B(\mathbf{u}, \mathbf{v}) = (\,\mathbf{f}, \mathbf{v})\end{aligned} \tag{4}$$

Equation (4) represents a continuous weak formulation, where $B(\cdot, \cdot)$ denotes an arbitrary bilinear form and $\mathbf{f}$ is a source function. The decomposition splits the original infinite dimensional function spaces into a coarse-scale (finite dimensional) space that corresponds to the finite element approximation space, and a complementary fine-scale space:

$$\mathscr{V} = \mathscr{V}_h \otimes \mathscr{V}' \tag{5}$$

The weak formulation itself may then be divided into one associated with the coarse-scale test functions, and one associated with the fine-scale test functions:

$$\begin{aligned}&\text{Find}\ \ \mathbf{u}_h, \mathbf{u}' \in \mathscr{V}_h \times \mathscr{V}'\ \ \text{s.t.}\ \ \forall\, \mathbf{v}_h, \mathbf{v}' \in \mathscr{V}_h \times \mathscr{V}':\\ &\begin{cases} B(\mathbf{u}_h, \mathbf{v}_h) + B(\mathbf{u}', \mathbf{v}_h) = (\,\mathbf{f}, \mathbf{v}_h) \\ B(\mathbf{u}', \mathbf{v}') = (\,\mathbf{f}, \mathbf{v}') - B(\mathbf{u}_h, \mathbf{v}') = (\mathscr{R}_{\mathbf{u}_h}, \mathbf{v}') \end{cases}\end{aligned} \tag{6}$$

where $\mathscr{R}_{\mathbf{u}_h}$ is the residual of the coarse-scale solution.

The weak formulation associated with the coarse-scale test functions, the first equation in (6), is the finite element formulation, including the terms that involve the fine-scale solution u'. These additional terms are the mechanism through which the scale interaction occurs and where a model must be adopted. This model can be developed based on the weak formulation corresponding to the fine-scale test functions, the second equation in (6) and results in:

$$\mathrm{u}' = \mathscr{G}'\left[\mathscr{R}_{\mathbf{u}_h}\right] \approx \tau\mathscr{R}_{\mathbf{u}_h} \tag{7}$$

where $\mathscr{G}'[\cdot]$ is the fine-scale Green's operator (Hughes and Sangalli, 2007), and τ is the parameter that appears after $\mathscr{G}'$ is approximated and its operation on $\mathscr{R}_{\mathbf{u}_h}$ is simplified (Brezzi et al., 1997).

Substitution of this fine-scale model into the finite element formulation, that is, $(*)$ in (6), yields a closed formulation that incorporates the scale interaction. The obtained finite element formulation is variationally consistent (i.e., it is satisfied by the exact solution), and the model parameters follow directly from the underlying equations and the approximation steps. In (Bazilevs et al., 2007), the following modeling terms were derived based on their residual-based variational multiscale turbulence model:

$$\begin{aligned} B^{VMS}(\mathbf{u}_h,\mathbf{v}_h) = {} & (\mathbf{u}_h\cdot\nabla\mathbf{v}_h + \nabla q_h, \tau_M\mathbf{r}_M(\mathbf{u}_h,p_h)) + (\mathbf{u}_h\cdot(\nabla\mathbf{v}_h)^T, \tau_M\mathbf{r}_M(\mathbf{u}_h,p_h)) \\ & -(\nabla\mathbf{v}_h, \tau_M\mathbf{r}_M(\mathbf{u}_h,p_h)\otimes\tau_M\mathbf{r}_M(\mathbf{u}_h,p_h)) + (\nabla\cdot\mathbf{v}_h, \tau_C r_C(\mathbf{u}_h)) \end{aligned} \tag{8}$$

with

$$\begin{aligned} \mathbf{r}_M(\mathbf{u}_h,p_h) &= \frac{\partial\mathbf{u}_h}{\partial t} + \mathbf{u}_h\cdot\nabla\mathbf{u}_h + \nabla p_h - \nu\nabla^2\mathbf{u}_h - \mathbf{f} \\ r_C(\mathbf{u}_h) &= \nabla\cdot\mathbf{u}_h \end{aligned} \tag{9}$$

which we add to the left hand side of (3) in our CFD computations. We use the following model coefficients from (Tezduyar and Osawa, 2000; Colomés et al., 2015):

$$\begin{aligned} \tau_M &= \left(\frac{4}{\Delta t^2} + \frac{4\left\|\mathbf{u}_h^2\right\|}{h^2} + \frac{16\nu^2}{h^4}\right)^{-1/2} \\ \tau_C &= \frac{h^2}{12\tau_M} \end{aligned} \tag{10}$$

with h and Δt being the characteristic element size and the time step size, respectively.

2.3. *Inflow boundary conditions with artificial incoming turbulence*

To obtain accurate computational solutions, the prescribed inflow boundary conditions must have turbulence characteristics that correspond to the physical system under investigation. A number of methods have been proposed to generate the turbulent boundary conditions artificially (Davidson and Billson, 2006; Di Mare et al., 2006). In this paper, we make use of the so-called synthetic eddy method (SEM) proposed by Jarrin et al. (2009) that is based on the Lagrangian treatment of vortices.

The SEM approach proposes to decompose the fluid in a superposition of different moving vortices. The domain of influence of each vortex is assumed to be a box. The velocity fluctuation at a point $\mathbf{x}$ that is influenced by N vortices (or eddies) can then be calculated by:

$$\mathbf{u}'_i(\mathbf{x}) = \frac{1}{\sqrt{N}}\sum_{k=1}^{N} a_{ij}\,\sigma_j^k\,f_\sigma^k\left(\frac{\mathbf{x}-\mathbf{x}^k}{s^k}\right) \tag{11}$$

where $\mathbf{x}^k$ is the location of the k^{th} eddy, s^k is the length scale of the eddy obtained from an empirical formula, and $f_\sigma^k(\mathbf{x})$ is a so-called shape function. The vector $\boldsymbol{\sigma}^k$ contains randomly assigned eddy intensities which obey a Gaussian distribution with zero mean value and a standard deviation of 1, and a_{ij} are the Lund coefficients defined as follows:

$$a_{ij} = \begin{bmatrix} \sqrt{R_{11}} & 0 & 0 \\ \dfrac{R_{21}}{a_{11}} & \sqrt{R_{22}-a_{21}^2} & 0 \\ \dfrac{R_{31}}{a_{11}} & \dfrac{R_{32}-a_{22}\cdot a_{31}}{a_{22}} & \sqrt{R_{33}-a_{31}^2-a_{32}^2} \end{bmatrix} \tag{12}$$

The Reynolds stresses R_{ij} are the remaining free parameters to calibrate (11). For details on how to calibrate and implement the SEM method, we refer the interested reader to (Jarrin et al., 2009). We illustrate the accuracy of the SEM method by comparing the mean flow magnitude and the root mean square of the velocity fluctuations with respect to corresponding results from wind tunnel experiments (see Section 3.2.2 for further details). Fig. 1a and b plot the results generated by the SEM against the wind tunnel results at a free-stream velocity of $U_\infty = 7.5$ m/s, demonstrating excellent agreement between model and experiment. We note that the quantities plotted in Fig. 1 refer to the classical law of the wall, a self similar solution for the mean velocity parallel to the wall that can be expressed as

$$u^+ = \frac{\overline{u}}{u^\star} = \frac{1}{\kappa}\ln y^+ + C^+, \quad \text{with } y^+ = \frac{yu^\star}{\nu} \tag{13}$$

where u^+ is the dimensionless velocity parallel to the wall, $u^\star = \sqrt{\tau_w/\rho}$ is the shear velocity (with τ_w and ρ being the wall shear stress and fluid density), y^+ is the dimensionless wall coordinate (with ν being the kinematic viscosity), and the von Kármán constant is $\kappa = 0.40$. The plotted results refer to a wind tunnel experiment, for which $u^\star = 0.24$ m/s and $C^+ = 5.5$. An alternative representation of the law of the wall that is often used to specify wind tunnel experiments is:

$$u(y) = u(y_{ref})\left(\ln\frac{y}{y_0}\middle/\ln\frac{y_{ref}}{y_0}\right) \tag{14}$$

where y_0 is the roughness length (the distance from the wall at which the idealized velocity given by the law of the wall goes to zero). In the current case, the roughness length is $y_0 = 7.3\cdot 10^{-6}$ m, the standard height $y_{ref} = 1.96$ m and the free-stream velocity is $U_\infty = u(y_{ref}) = 7.5$ m/s.

2.4. *FEniCS as a platform for high-performance computing*

We implemented the above methods within the open-source computing platform FEniCS (Logg et al., 2012). FEniCS supports MPI, a computing protocol for distribution on a parallel high-performance computing cluster. To handle large systems of equations, we require an iterative solver that scales well with the number of CPU cores. Good scaling of the linear solver relies on suitable preconditioning of the equation system. We found that the Jacobi preconditioner is sufficiently effective for the momentum equation. The equation for the pressure may roughly be regarded as a Poisson equation, for which we used an algebraic multigrid preconditioner (Yanget al., 2002). Our framework exhibits good strong scaling, achieving a parallel efficiency of 91.6% at 192 cores.

3. Computational prediction and experimental validation of road sign aerodynamics at the laboratory scale

In this section, we briefly describe a real-world road sign structure, operated by the Minnesota Department of Transportation. We then explore the aerodynamic characteristics of this specific road sign experimentally in the towing tank and the wind tunnel of the St. Anthony Falls Laboratory, using a scaled model. We validate our CFD framework by computationally predicting the range of experimentally measured aerodynamic quantities for the scaled model.

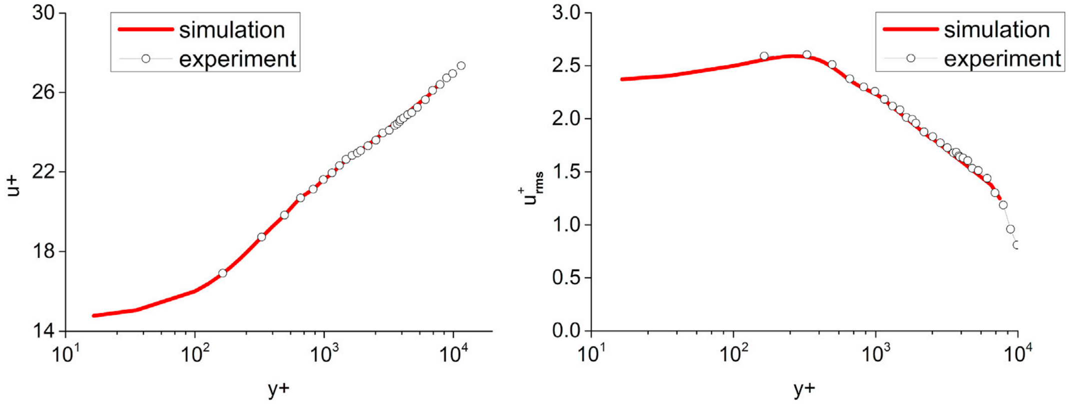

(a) Dimensionless mean velocity u^+ parallel to the wall **(b)** Corresponding root mean square u^+_{rms}

Fig. 1. Comparison of results from the SEM method and the wind tunnel experiments. The definitions of the plotted quantities are given in (13).

3.1. The RICWS structure deployed by the Minnesota Department of Transportation

Rural intersection conflict warning signs (RICWS) operated by the Minnesota Department of Transportation (MnDOT) are installed at high risk intersections to warn drivers who are approaching from a minor roadway of high speed traffic that travels on the major roadway. They feature a diamond-shaped electronic messaging panel in the center and yellow flashing lights at the top. Fig. 2 illustrates the original RICWS configuration and its dimensions. We note that we report dimensions in USCS units, in which the RICWS is designed, but use SI units otherwise.

Since the RICWS is installed in direct vicinity to the road, it features breakaway mechanisms. When a vehicle impacts the sign, the impacted lightweight posts will fracture, bend, or pull from the ground, allowing the vehicle to pass through the sign with minimal damage to the vehicle (McGee, 2010). Due to the relatively soft support structure, the RICWS exhibits pronounced vibrations when excited by wind loading. A possible solution is the stiffening of the support structure. Adding stiffness in the direction of approaching vehicles, however, would remove the breakaway status of the RICWS, which is therefore not a viable option for MnDOT.

3.2. Scaled model in the laboratory

To validate our CFD framework for aerodynamic analysis of the RICWS, its aerodynamic behavior is first explored via experiments that were conducted with a small-scale model in the main channel and the wind tunnel at the St. Anthony Falls Laboratory of the University of Minnesota. The scaled model of the RICWS and its dimensions are shown in Fig. 3. It was fabricated from stainless steel at a scale of 1:18. Due to fabrication reasons, the plate thickness was kept at 0.25 in.

3.2.1. Drag experiments in the towing tank

To identify drag properties of the RICWS and its primary shedding frequency, we conducted drag experiments that are illustrated in Fig. 4. Both the instrumentation and the model were attached to a data acquisition cart that tows the submerged model at a specified speed. Since the channel can be considered a still water basin, the flow relative to the model is spatially uniform. Force measurements were sampled at 50 Hz while the model was towed.

From the results of the drag experiments, we can compute the drag coefficient C_d defined as

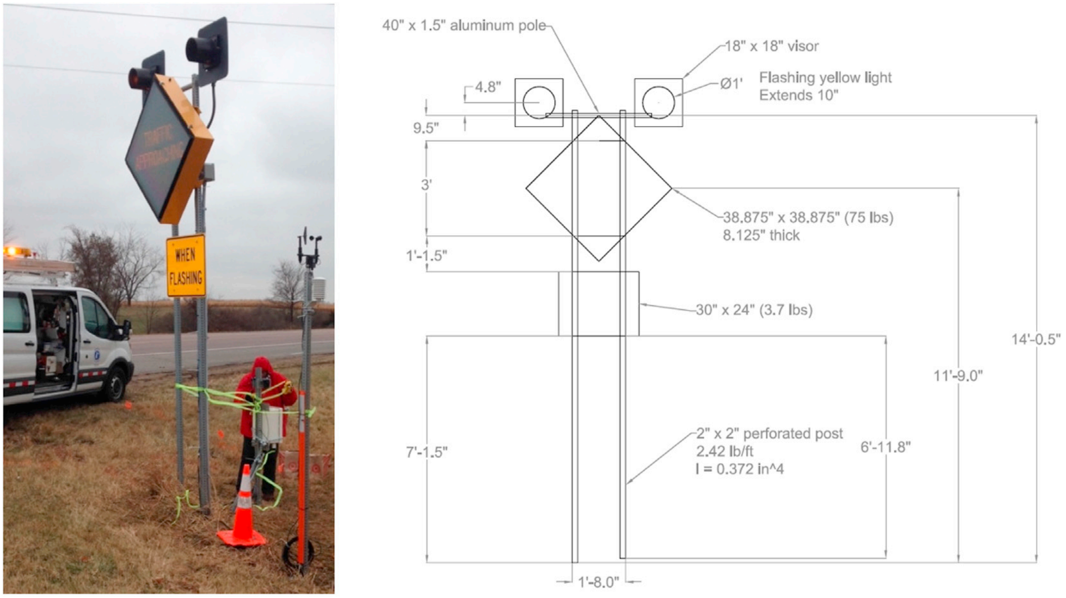

(a) RICWS in the field. **(b)** CAD drawings (dimensions in USCS units, courtesy of MnDOT).

Fig. 2. Rural intersection conflict warning sign (RICWS) operated by the Minnesota Department of Transportation.

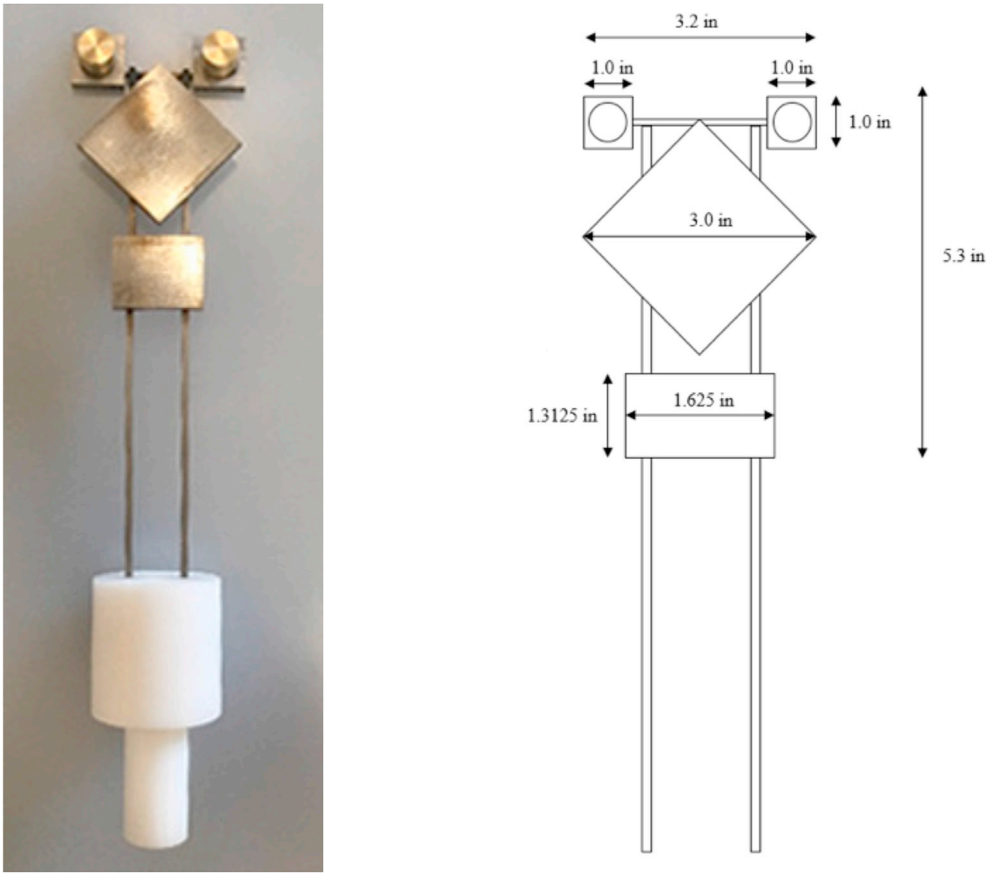

(a) Scaled model.

(b) Dimensions in USCS units.

Fig. 3. Scaled model of the RICWS that was used in the experiments at the St. Anthony Falls Laboratory.

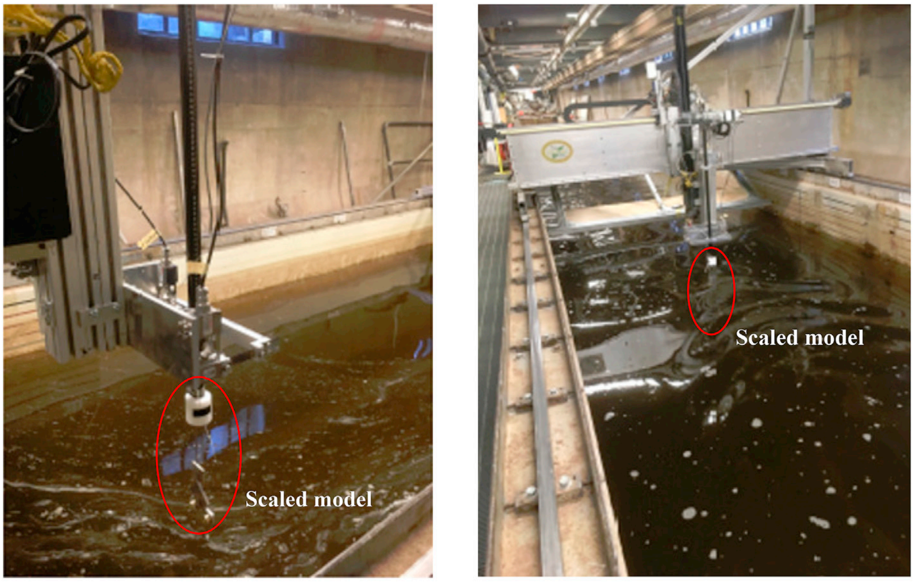

(a) Scaled model before submergence.

(b) Submerged model on data acquisition cart.

Fig. 4. Drag experiment set-up in the main channel facility at the St. Anthony Falls Laboratory.

$$C_d = \frac{F_d}{\frac{1}{2}\rho u^2 A_d} \tag{15}$$

It quantifies the resistance of an object in a flow, where F_d is the force component in the direction of the flow, ρ is the mass density of the fluid, u is the homogeneous upstream velocity (here the towing velocity of the RICWS model relative to the resting fluid in the channel), and A_d is a reference area (here the projected vertical area of panels and lights). The Strouhal number defined as describes oscillations under flow normal to the sign, where f_s is the shedding frequency (for the RICWS model identified by spectral analysis of the measured drag force component parallel to the flow direction), and L is the characteristic length (for the RICWS model the horizontal length across the diamond plate). The dimensionless numbers and associated quantities derived from the experimental results are summarized in Table 1. We observed that C_d and St are independent of the Reynolds number for the range of tow velocities tested.

$$St = \frac{f_s\, L}{u} \tag{16}$$

3.2.2. Wake experiments in the wind tunnel

To characterize the vertical wake profiles that result from the inflow turbulent boundary layer, we conducted wake experiments in the closed-loop boundary layer wind tunnel at the St. Anthony Falls Laboratory. The facility features a turbulence trip at the leading edge of the tunnel that disturbs the air flow in the tunnel and develops a turbulent boundary layer. In the current experiments, a free-stream velocity of $U_\infty = 7.5$ m/s was chosen. The scaled RICWS model was mounted to the floor of the wind tunnel upstream of a hot-wire anemometer system on a motorized traverse system. More details on the experimental set-up that is shown in Fig. 5 can be found in (Howard et al., 2016).

The measurements illustrate the vertical wake profiles for the generated inflow boundary layer, describing the variation in velocity with respect to height within the downstream wake of the RICWS model. The downstream wake distance of the three measurement locations is normalized by H, the vertical distance from the bottom of the lowest plate to the top of the highest plate on the RICWS model as illustrated in Fig. 6. For each measurement location, data was collected for 75 s at a sampling rate of 10,000 Hz. At each location, the mean velocity profiles and the root mean square (RMS) can be computed. Fig. 7 plots the measured mean velocity and RMS profiles for the main wind direction perpendicular to the sign panels. In addition, Reynolds stresses of the inflow turbulent boundary layer were measured as an input parameter for the SEM model that accounts for incoming turbulence in our CFD framework.

The largest turbulent eddies generated in the wind tunnel or occurring in the atmospheric surface layer scale in size with the boundary layer thickness δ (Balakumar and Adrian, 2007), specifically 6δ (Guala et al., 2006, 2011). In our wind tunnel experiments, the thickness was approximately $\delta = 0.6$ m. We can estimate the turnover time of the largest eddies using the free-stream velocity of the experiment $U_f = 7.5$ m/s, leading to the turnover time $T = 6\delta/U_f \sim 0.5$ s. In this context, the measurement duration of 75 s is equivalent to over 150 turnover time scales, which is much more than the 20 turnover times typically used for estimating first- and second-order velocity statistics in addition to turbulence spectra. Assuming similar velocity conditions and a surface layer thickness in the order of 100 m, the very large turnover time scale in the field is around 60 s, requiring about 20 min of measurements, which is within the typical range of averaging times for the Reynolds decomposition on flat terrain.

There are, however, a few limitations to acknowledge: the height of the RICWS model normalized with δ is not conserved. It is much larger in the wind tunnel as compared to the field scale. This implies that the ratio between model and field time scales changes if we consider the length scale ratio of the RICWS $(1/18)$, or the boundary layer thickness ratio $(\sim 1/200)$. Due to the limitations in computational resources, a choice must be made on the spatial domain in which the RICWS is simulated. Since the domain cannot vertically extend to the thickness δ of the atmospheric surface layer or allow the generation of δ-scale motions in the streamwise direction, the incoming flow conditions will ensure the correct mean shear but not all the variability of atmospheric turbulence. With this statement in mind, the spatio-temporal domain of the simulation must be designed to resolve the wake oscillations comprised of many turnover time scales, which are not based on the turbulence of the incoming flow, but rather on the vortex shedding and on the oscillation period of the structure. In this context, the simulation time, at equilibrium, is not expected to cover the averaging time of atmospheric turbulence, but to be $\sim 20L/U_f$, where L is the length of the domain in streamwise direction or O (10) times the natural period of the RICWS.

Table 1
Comparison of aerodynamic characteristics for the towing tank test at a relative flow speed of $u = 0.5$ m/s.

	Experimental results	Computational results
Mean drag force F_d	0.937 N	0.953 N
Drag coefficient C_d	1.34	1.37
Shedding frequency f_s	1.31 Hz	1.2 Hz
Strouhal number St	0.20	0.18

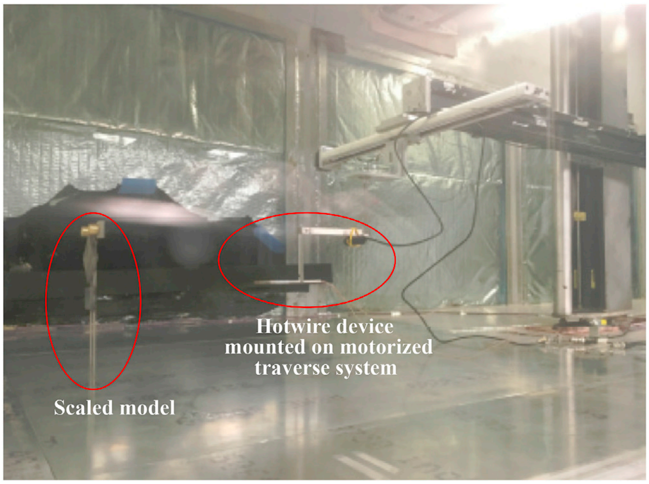

Fig. 5. Wake experiment set-up in the closed-loop boundary layer wind tunnel at the St. Anthony Falls Laboratory.

3.3. CFD model validation

Using the available experimental data, we perform an extensive validation study with our CFD framework. For all lab-scale computations, we discretize a box of 1.17 m × 0.453 m × 0.6 m (stream, wall-normal and cross directions, respectively) around the panels of the sign structure. We neglect the slender beam components of the support structure in our CFD simulations, as their flow resistance are significantly smaller than the resistance of the panels. Using the commercial tool ANSYS ICEM (ANSYS Inc, 2015), we carefully design a mesh that adaptively resolves all boundary layers to reliably capture their flow characteristics. Fig. 6 plots the elements on the central vertical plane of the box in streamwise direction. Mesh refinement concentrates at the lower wall, around the sign object (characteristic element size $h = 7 \times 10^{-4}$ m) and in the wake region ($h = 8 \times 10^{-3}$ m). The remaining regions are discretized with $h = 1 \times 10^{-2}$ m. The resulting mesh consists of 12 million tetrahedral elements, equipped with linear nodal basis functions.

We use the same mesh with different boundary conditions and fluid properties of water and air (temperature 15 °C, atmospheric pressure) for the simulation of the towing tank and wind tunnel scenarios, respectively. In each case, we compute 8 s of flow history at a time step size of $4 \cdot 10^{-4}$ s. As an initial condition we use the solution to a Stokes problem. We distribute our code on 360 cores, resulting in a simulation time per time step of 11.0 s. To simulate the towing tank case, we assume a constant inflow velocity of $u = 0.5$ m/s at the inlet boundary. If we assume H as the characteristic length scale, this results in a Reynolds number of $Re_H = 5.85 \times 10^4$. The imposed conditions at the outflow boundary and at all boundaries along the streamwise direction are zero pressure and symmetry boundary conditions, respectively. At the

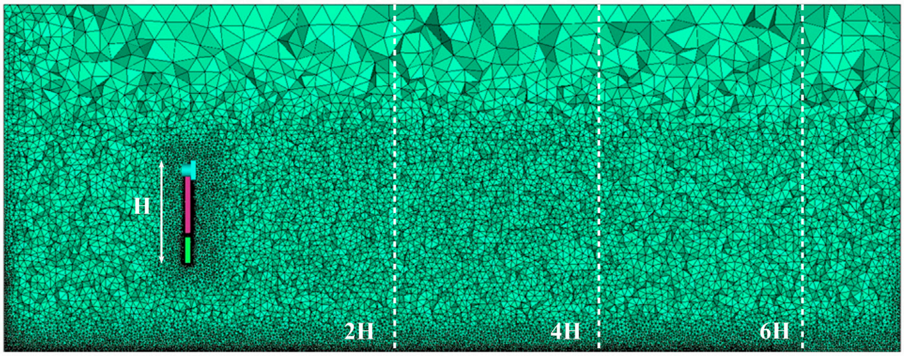

Fig. 6. Mesh for the lab-scale CFD computations. The dotted white lines denote the measurement locations of the mean and root mean square velocity profiles in the wake.

surfaces of the RICWS model, no-slip conditions are imposed. After time averaging, we derive the aerodynamic key characteristics summarized in Table 1. We observe that the computational results reproduce the results of the drag experiments well.

To simulate the wind tunnel case, the inlet boundary conditions are imposed according to the artificial turbulence model described in Section 2.3, with parameters associated to the validation study of Fig. 1. With a free-stream velocity of $U_\infty = 7.5$ m/s, we obtain a Reynolds number of $Re_H = 6.9 \times 10^4$, which is in the same order as for the towing tank case. All other boundary conditions remain unchanged. Fig. 7 plots the time-averaged mean velocity and root mean square profiles evaluated from the computational solution. We observe that they agree very well with the corresponding experimental data, confirming that our CFD framework produces results that capture key characteristics of the flow. In particular, this includes the high velocity gradient at the boundary layer and the mean velocity profile at various distances in the wake of the sign object. In addition, the turbulent behavior of the flow, represented by the fluctuations in terms of the root mean square, represents the measured profiles very well.

Following the good fit of experimental and computational results for the towing tank and wind tunnel cases, we can consider our computational framework to be validated successfully. We note that we conducted a mesh convergence study to reconfirm that the current discretization represents an appropriate compromise between computational efficiency and sufficient convergence of the key flow characteristics examined here.

4. Computational exploration of aerodynamic modifications at the field scale

We now proceed to simulate the aerodynamic response of the original RICWS structure by scaling the validated CFD model to the field scale. Using the simulated pressure history on the panel surfaces, we obtain the vibration response from a computational structural dynamics model in Abaqus. Our study focuses on the critical case of head wind in the traveling direction of passing vehicles. For tail wind, adding directional support mechanisms could increase the stiffness and hence the vibration resistance of the sign. For wind that arrives at an angle to the sign, the two posts form a frame structure parallel to the panels, such that the vibration resistance at an angle is much larger than in the head wind direction. We motivate two potential modifications of the original RICWS configuration, one based on the removal of the two top panels and one based on the addition of rear extensions behind the main diamond-shaped panel. Fig. 8 shows the three RICWS configurations examined in the following. After repeating the same computational procedure, we compare and assess the aerodynamic and vibration response for each RICWS configuration.

4.1. *Computational aerodynamic analysis of the field-scale structure*

To arrive at the field-scale, we scale the finite element discretization of the (validated) lab-scale box by a factor of 18, which warrants some careful considerations. First, we need to determine a critical upstream wind speed to excite the sign structure. From a practical viewpoint, we are interested in choosing a wind speed that corresponds to the standard wind condition in the more populated southern areas of Minnesota, where the RICWS is typically deployed. Fig. 9 plots average wind speed estimates at 30 m provided by the National Renewable Energy Laboratory for Minnesota. Using this data as a rough guideline, we choose an inflow wind speed of $u = 7$ m/s, which we interpret as the mean inflow velocity at a height of 3 m. The complete mean velocity profile can then be constructed by calibrating the inflow velocity to obey the logarithmic law of the wall (Schlichting and Gersten, 2016). From the ASCE building code 7–10, we can pick a surface roughness of $y_0 = 0.03$ m that holds for open terrains. We then can fit the law of the wall by fitting the logarithmic distribution to the mean velocity $u = 7$ m/s at 3 m, finding a shear velocity of $u^\star = 0.608$ m/s. The remaining boundary conditions are equivalent to the wind tunnel simulations.

For the representation of incoming turbulence via the SEM model, we do not have measurement data at the field scale. We therefore use the input data from the lab-scale wind tunnel simulations. The ASCE building code 7–10 that specifies wind loading (Simiu, 2011) provides relations between the variance of the flow in different flow directions and the shear velocity $u^\star$, which follows from the mean flow profile. Using our calibrated logarithmic velocity distribution at the inflow, we find a streamwise variance of $4(u\star)^2$, a wall-normal variance of $1.5(u^\star)^2$, a spanwise variance of $3(u^\star)^2$, a Reynolds shear stress of $R_{1,2} = -(u^\star)^2$ and the remaining terms $R_{1,3} = R_{2,3} = 0$. The lab-scale input parameters to the SEM model are likely to represent over-predictions, leading to localized non-physical flow features in the vicinity of the inflow boundary.

With the inflow velocity and boundary layer calibration in place, we can determine a field-scale Reynolds number of $Re_H = 1.15 \times 10^6$ that is more than one order higher than the Reynolds numbers in the lab-scale validation study. We therefore expect boundary layers at the ground and the panels that are thinner than in the lab-scale cases, requiring a finer mesh resolution. As a consequence, starting with the lab-scale mesh size shown in Fig. 6, we initiate further refinement in the boundary layer regions, leading to a field-scale mesh of 15 million tetrahedral elements. Adaptive mesh refinement is illustrated in Fig. 10, where elements on a central vertical and a central horizontal plane are plotted. We compute 45 s of flow history, where we assume the result of Stokes flow as an initial condition and use a time step of 1×10^{-3} s. Only the diamond sign is modeled as a volumetric object, while the remaining panels above and

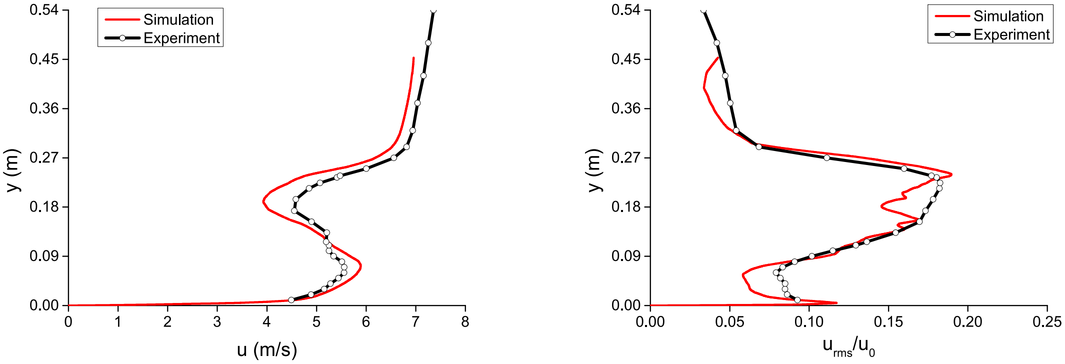

(**a**) Streamwise mean velocity at $2H$. (**b**) RMS of streamwise velocity at $2H$.

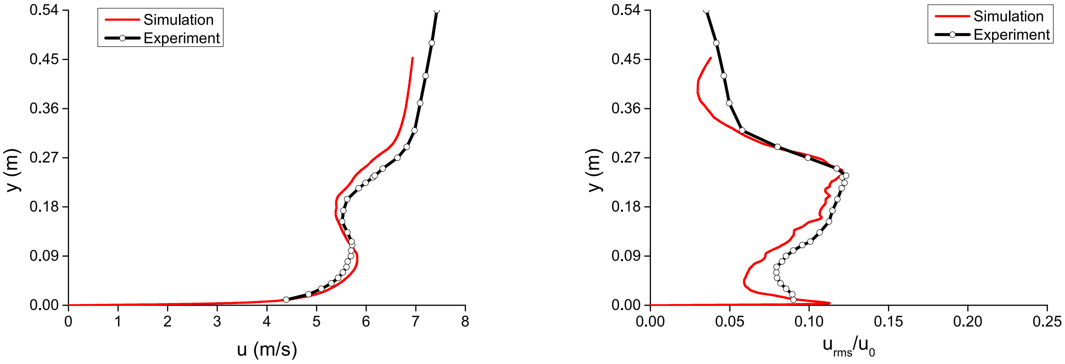

(**c**) Streamwise mean velocity at $4H$. (**d**) RMS of streamwise velocity at $4H$.

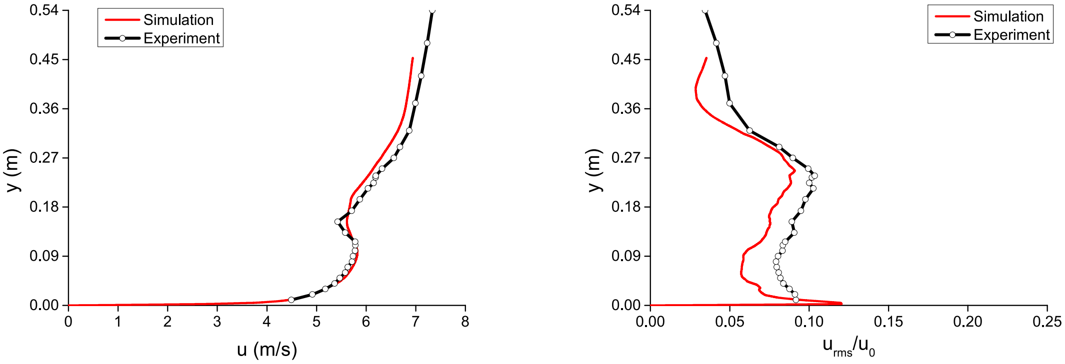

(**e**) Streamwise mean velocity at $6H$. (**f**) RMS of streamwise velocity at $6H$.

Fig. 7. Comparison of the results for the streamwise velocity at three different wake locations, obtained from the wind tunnel experiments and the CFD simulation. As illustrated in Fig. 6, the wake locations are parametrized in terms of H (vertical distance from the bottom of the lowest plate to the top of the highest plate).

below are considered thin surfaces without volume. We note that this deviates from the CFD model for the laboratory scale simulations, where all panels and lights were represented by volumetric objects. For efficient parallel computing, we use 480 cores on the Mesabi cluster of the Minnesota Supercomputing Institute, leading to a wall-clock time per time step of 13 s.

The resulting flow fields are illustrated in Figs. 11a, 12a and 13a with plots of the (instantaneous) vorticity, the mean velocity and the turbulent kinetic energy, respectively. The vorticity profile in Fig. 11a visualizes the vortices that are generated by the panels in the wake region. Figs. 12a and 13a confirm the wake region, accompanied by flow separation, turbulence and vortex shedding.

4.2. *Computational structural analysis of wind-induced vibrations*

To be able to assess the vibration behavior of the RICWS structure that results from the simulated aerodynamic response, we transfer the transient pressure data on the surfaces of the sign panels that are obtained via the CFD simulations into displacement data of the structure. To this end, we consider a structural dynamics model of the RICWS structure in the commercial finite element software Abaqus (Dassault Systèmes, 2013). The model whose geometry is illustrated in Fig. 14a is based on the CAD drawings provided by MnDOT (see Fig. 2) and consists of standard shell and beam elements for the panels and columns, respectively, where the different structural components are coupled using multi-point

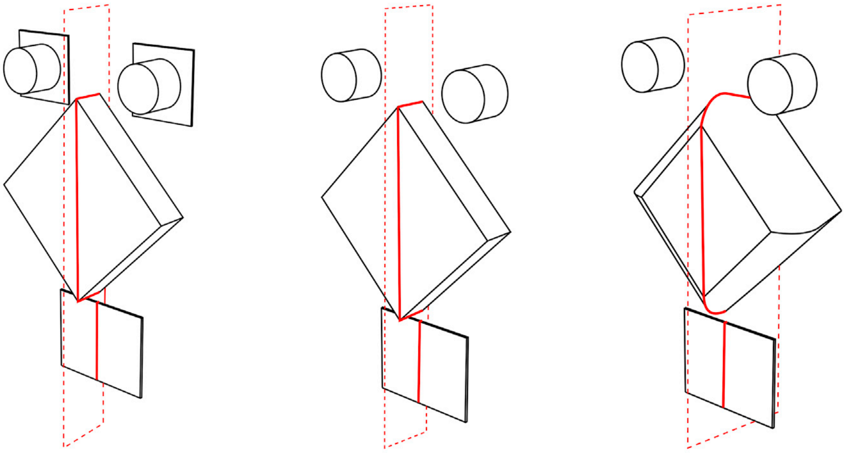

(a) Original RICWS configuration operated by MnDOT.

(b) Modification 1 (removal of top panels).

(c) Modification 2 (addition of rear extension to diamond panel).

Fig. 8. The original RICWS configuration vs. two possible modifications that reduce drag and vibration sensitivity. The red lines illustrate the central plane on which we will plot simulated flow field results. (For interpretation of the references to colour in this figure legend, the reader is referred to the Web version of this article.)

constraints. The boundary conditions at the lower ends of the two posts are fixed. The material is steel with Young's modulus $E =$ 20,000 MPa and Poisson's ratio $\nu = 0.3$. All panels are modeled by rigid shell elements such that local plate deformation modes are avoided.

Fig. 14b illustrates the three lowest eigenfrequencies and the corresponding eigenmodes. The critical lowest mode is at 1.0 Hz and corresponds to bending in the streamwise flow direction. The critical eigenfrequency and eigenmode are confirmed by experimental tests carried out on the real structure in the field and reported in (Finley, 2018). Following prior studies (Constantinescu et al., 2007; Beneberu et al., 2014; Lottes et al., 2011), we employ one-way coupling, where pressure is calculated on the undeformed sign at all times, with the understanding that the vibration amplitude at the chosen moderate wind speed is much smaller than the characteristic length scale of the sign. The pressure data from the fluid flow computations is projected onto the sign structure by linear interpolation onto the integration points of the structural model. To simulate the dynamic response, we use an implicit time integration scheme with a time step size of $1 \cdot 10^{-3}$ s for a total of 45 s. We choose the undeformed configuration of the sign as the initial condition. The structural model assumes Rayleigh damping. The mass-proportional damping coefficient η and the stiffness-proportional damping coefficient δ can be determined from

$$\delta = \frac{2\xi}{\omega_1 + \omega_3}\ , \quad \eta = \omega_1 \omega_3 \delta \tag{17}$$

where ω_1 and ω_3 are the first and third eigenfrequencies of the structure, if the critical damping ratios ξ in both first and third modes of vibration of the structure are set equal (Wilson, 2010). The critical damping ratio is set to $\xi = 1\%$, which is a common assumption for steel structures. For the original sign configuration, this procedure results in $\delta = 6.241 \cdot 10^{-4}$ s and $\eta = 0.101$ s^{-1}.

Fig. 15a plots the displacement history evaluated at the top point of the diamond panel. We observe that the dominant oscillatory mode corresponds to the first eigenfrequency at 1.0 Hz. This observation is confirmed by Fig. 15b that shows the modal amplitudes of the displacement response, obtained via a fast Fourier transform of the displacement data, that spikes at 1.0 Hz. The Abaqus results confirm that the RICWS exhibits a pronounced sensitivity to vibrations due to the excitation of the first eigenfrequency, correlating to our observations of the real RICWS in the field.

4.3. *Removing secondary panels at the top*

Our objective is to effectively dampen wind-induced vibrations without adding stiffness to the support structure. Of particular interest are inexpensive and simple changes in the currently used configuration of a sign structure. For the current example, one idea is to remove the vertical panels around the flashlights at the top. These top panels act as additional drag resistance and, despite their relatively small area, have an impact on the dynamic behavior of the structure, because they are far away from the support, adding considerable extra moment. To corroborate this hypothesis, we consider the modified RICWS configuration without top panels, illustrated in Fig. 8b.

Repeating the same computational analysis procedure as detailed above, we first compute the aerodynamic response with our CFD framework, taking into account the modified geometry, and then compute the vibration response with a modified Abaqus model. The resulting (instantaneous) vorticity, mean velocity and the turbulent kinetic energy are plotted in Figs. 11b, 12b and 13b, respectively. Compared to the results for the original RICWS configuration, we can observe local differences in the flow fields near the top of the diamond-shaped main panel. These observations indicate that the removal of the top panels enables a smoother flow around the structure, with a free shear layer that shows little deviation from the free-stream streamlines. Considering the overall field characteristics, however, we observe that in comparison to the results for the original configuration, the flow fields do not change significantly when the top panels are removed, both in terms of the spatial distribution as well as their maximum values.

Fig. 15a and b plot the displacement history of the top point of the diamond panel and the corresponding modal amplitudes, respectively, that are obtained from the structural dynamics simulation in Abaqus. We see from the spike in Fig. 15b that the critical eigenfrequency of the modified structure shifts to a slightly higher value compared to the original RICWS, since the weight of the top panels is removed, while the stiffness of the structure remains the same.

4.4. *Adding rear extensions to the main panel*

We explore a further modification, illustrated in Fig. 8c, based on the addition of rear extensions to the diamond-shaped sign panel that is responsible for most of the drag. This idea is motivated by the recent success of rear extensions in reducing the drag of trailer trucks (Storms

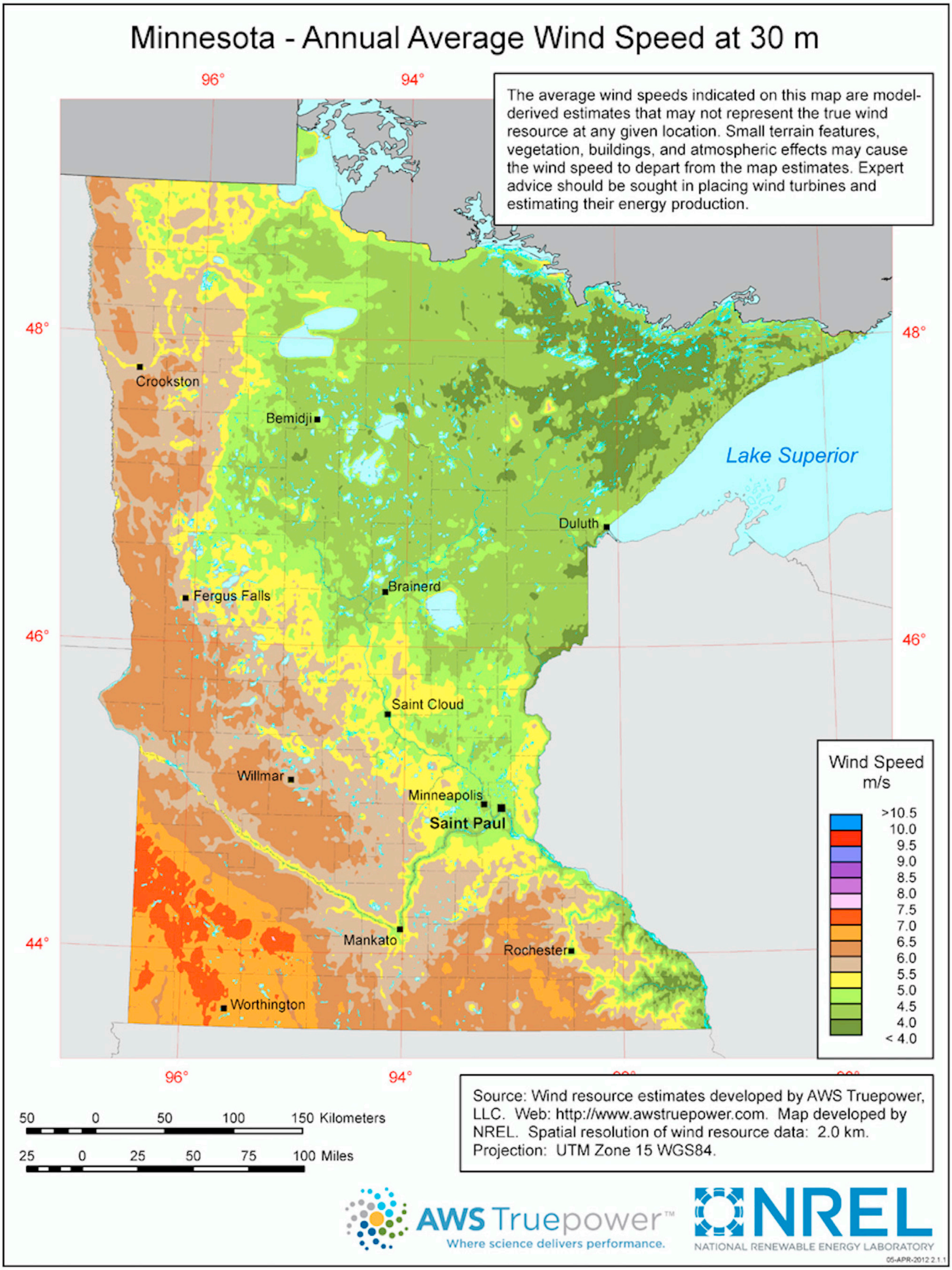

Minnesota - Annual Average Wind Speed at 30 m

The average wind speeds indicated on this map are model-derived estimates that may not represent the true wind resource at any given location. Small terrain features, vegetation, buildings, and atmospheric effects may cause the wind speed to depart from the map estimates. Expert advice should be sought in placing wind turbines and estimating their energy production.

Source: Wind resource estimates developed by AWS Truepower, LLC. Web: http://www.awstruepower.com. Map developed by NREL. Spatial resolution of wind resource data: 2.0 km. Projection: UTM Zone 15 WGS84.

Fig. 9. Average annual wind speeds at 30 m across the state of Minnesota, provided by AWS True power and NREL. Retrieved from WINDExchange, U.S. Department of Energy: https://windexchange.energy.gov/maps-data/194.

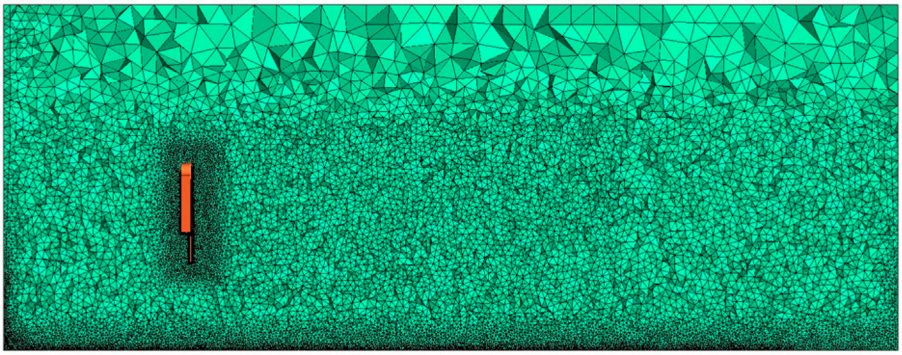

(**a**) Mesh in the central plane.

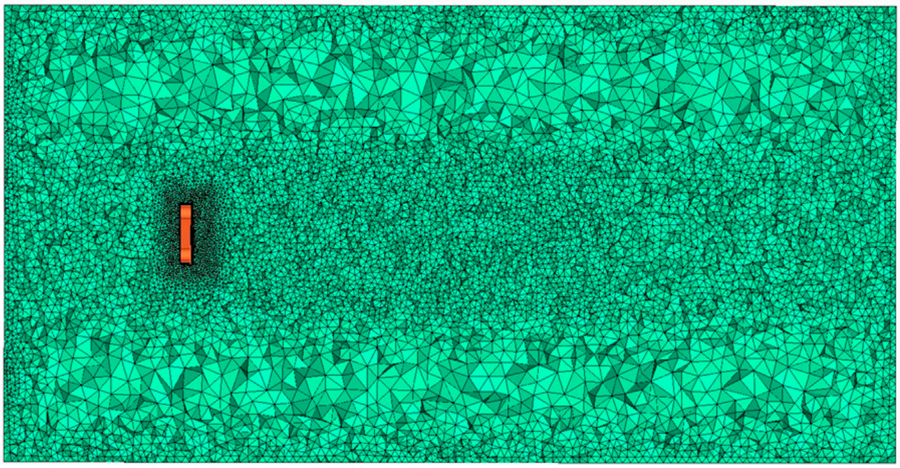

(**b**) Mesh in the crosswise plane.

Fig. 10. Mesh for the field-scale CFD computations.

et al., 2004; Browand et al., 2005; Håkansson and Lenngren, 2010). In the original configuration, the flow separation at the sharp edge of the diamond panel results in a disruption of the flow, which in turn results in a pressure drop across the sign panel. To reduce this pressure drop, we install four flat flaps at the trailing edge of the diamond panel. These flat plates have a length of one third of the diagonal of the diamond panel and are angled inwards by 15° with respect to the normal of the panel. The inclination angle is chosen according to optimization studies with different angles in rear extensions of trailer trucks (Browand et al., 2005; Håkansson and Lenngren, 2010). Their purpose is to move the point of flow separation backwards and to improve the overall flow stability of the airflow around the structure. Fig. 16 shows front and side views of the resulting modified configuration of the panels and flashlights. To avoid additional sharp edges that could initiate flow separation, we round out all connection lines of the flaps to each other and to the diamond panel by fillets. We note that the area of the modified diamond panel projected onto a vertical plane remains the same as the area of the original RICWS configuration. The space enclosed by the four flaps remains open, since their rear edges are not joined together.

The (instantaneous) vorticity, mean velocity and the turbulent kinetic energy that result from the CFD simulation are plotted in Figs. 11c, 12c and 13c, respectively. Compared to the results for two previous configurations, we observe that all flow fields exhibit larger changes. The wake region and the turbulent eddy intensity behind the diamond panel are now clearly reduced, indicating a reduction in the flow disruption. It is interesting to note that the wake region and the turbulent kinetic energy remain almost unaltered for the region behind the lower sign panel that has not been equipped with a drag reduction device. This may potentially be improved by using different angles of the drag reduction flaps or by installing a similar device on the lower panel.

The results of the structural dynamics simulation are plotted in Fig. 17. We observe that the addition of the drag reduction device behind the diamond panel yields a clear reduction of the vibration response. This reduction is reflected in the decrease of the modal amplitude at the first eigenfrequency in Fig. 17b.

4.5. *Assessment of aerodynamic modifications*

In the following, we compare and assess the three RICWS configurations based on their computational analysis. In Table 2, the drag force averaged over the complete time history of 45 s and the corresponding drag coefficient for each sign configuration are summarized. The reference quantities involved are the inflow velocity $u = 7$ m/s and the vertical streamwise area $A_d = 1.86$ m^2 for the original RICWS and $A_d = 1.59$ m^2 for both modified configurations. We observe that the relative reduction of the mean drag force due to the removal of the top panels is 25% with respect to the original configuration. The addition of rear extensions to the diamond-shaped main panel contributes another 30%. The drag reduction is confirmed by the vorticity snapshots in Fig. 11, which can be seen as an indicator for drag. We observe that the drag coefficient computed with the field-scale simulation results agrees well with the drag coefficient determined experimentally at the lab scale (see Table 1). For both modified configurations, the drag coefficient indicating aerodynamic resistance per given area is lower compared to the original RICWS.

In Tables 3 and 4, we summarize the averaged lift force and pitching moment and the corresponding coefficients for each sign configuration. For the pitching moment, the reference quantity is defined as $R_M = 1/2\rho u^2 A_d h_d$, where h_d is the height of the geometric center of the diamond plate. We observe that the lift increases by almost a factor of 4,

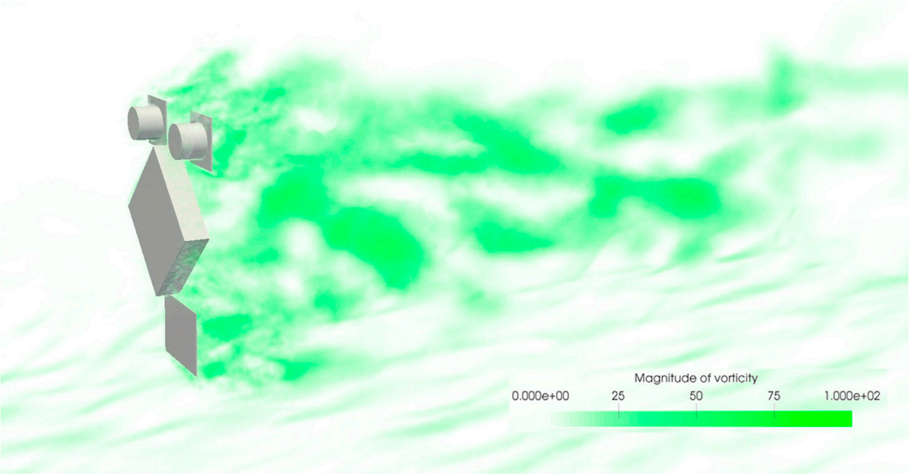

(a) Original RICWS configuration.

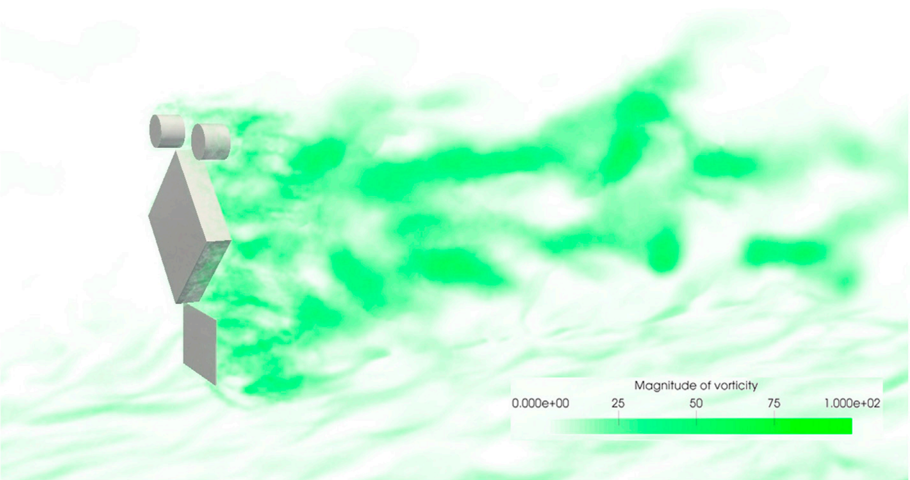

(b) Removal of top panels at flashlights (modification 1).

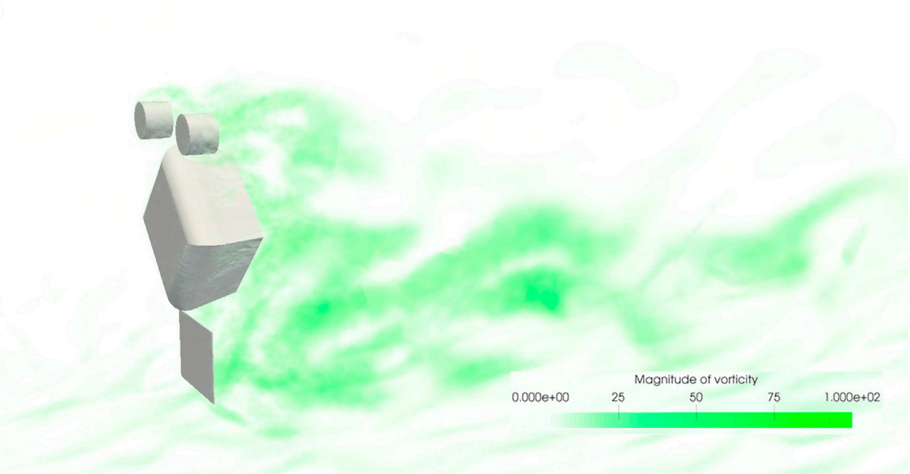

(c) Addition of rear extensions of diamond-shaped panel (modification 2).

Fig. 11. Vorticity snapshots associated with turbulence and hence increased drag. The unit of vorticity is 1/s.

when we add rear extensions, but remains a minor consideration when compared to the size of the drag.

Table 5 summarizes the corresponding vibration response for each configuration. Due to the linearity of the structural model, we can split the vibration response plotted in Figs. 15 and 17 into a "static" mean deflection that corresponds to the mean pressure loading, and a "dynamic" part that consists of zero-mean oscillations. The mean deflection of the original RICWS is 17.81 mm, which is reduced by 21% in modification 1 and by another 37% in modification 2. We thus observe that the reduction in drag force directly correlates with the reduction in mean

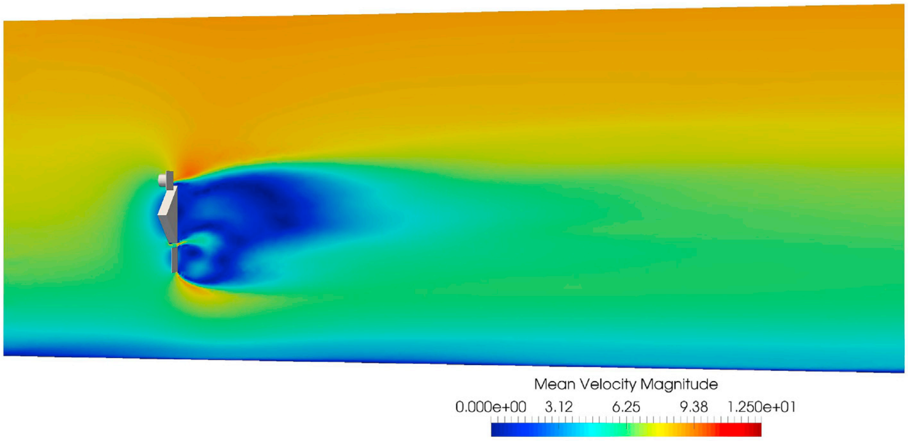

(a) Original RICWS configuration.(unit: m/s)

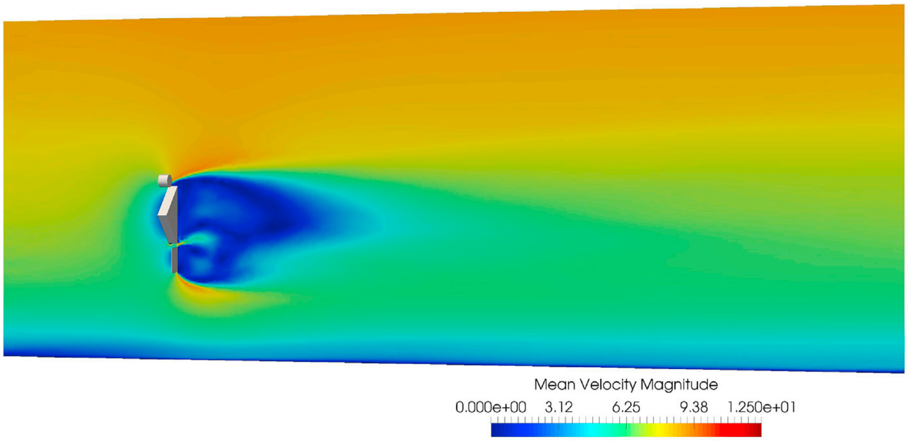

(b) Removal of top light panels (modification 1).

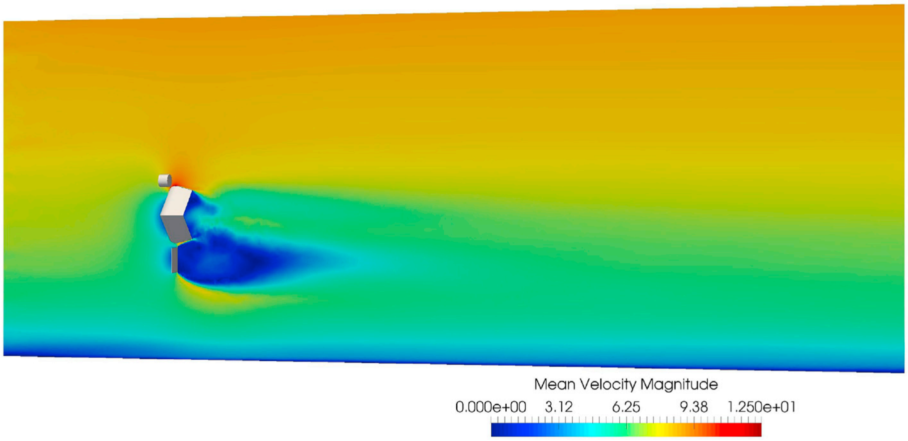

(c) Addition of drag reduction device at diamond panel (modification 2).

Fig. 12. Mean velocity (in m/s), averaged over later 80% of time history and plotted on the central vertical plane.

deflection. The dynamic part is characterized by the averaged zero-mean peak-to-peak amplitude of the oscillations. The amplitude of the original RICWS is 41.15 mm, which confirms that at the chosen moderate wind speed vibrations already dominate the displacement behavior in comparison to the mean deflection. For modification 1, however, the peak-to-peak amplitude reduces by only 7%, while for modification 2, it reduces by 48%. We thus have to conclude that the vibration behavior does not correlate with drag reduction alone.

In this study, we have considered fluctuating wind forces on the different sign structures which arise due to the upstream turbulence and

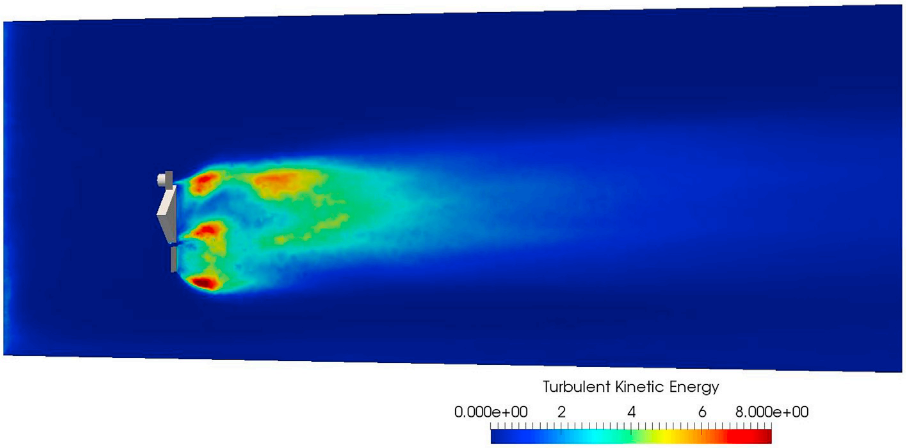

(a) Original RICWS configuration.

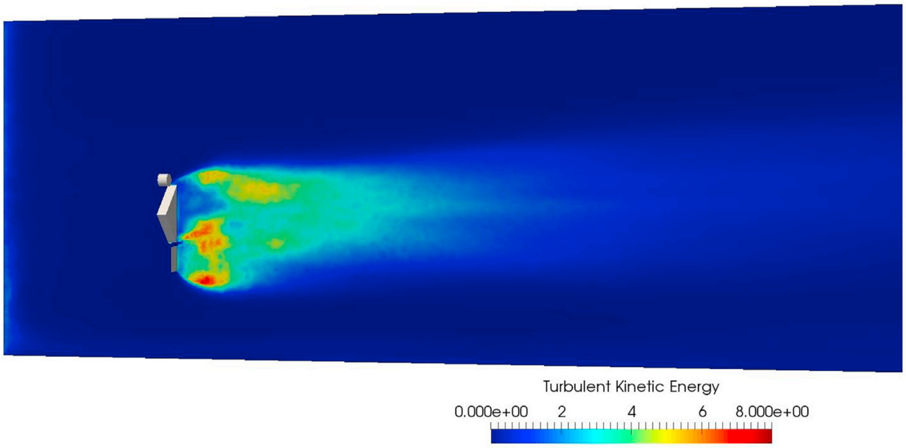

(b) Removal of top light panels (modification 1).

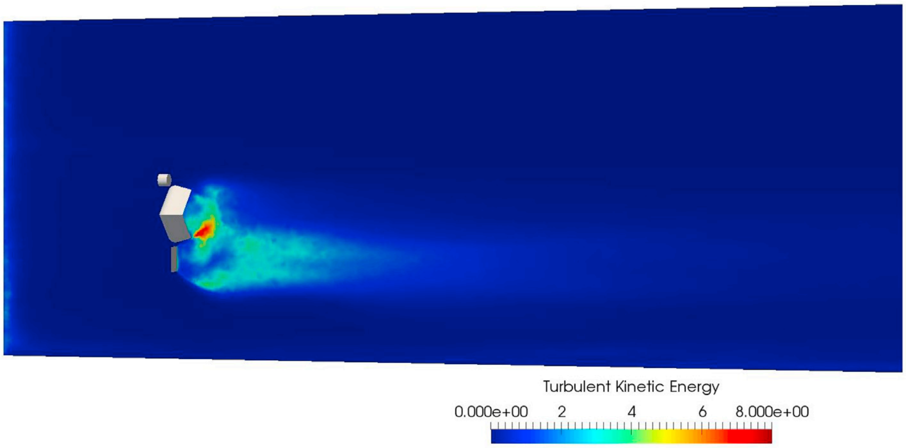

(c) Addition of drag reduction device at diamond panel (modification 2).

Fig. 13. Turbulent kinetic energy (in m/s), averaged over later 80% of time history, plotted on the central vertical plane.

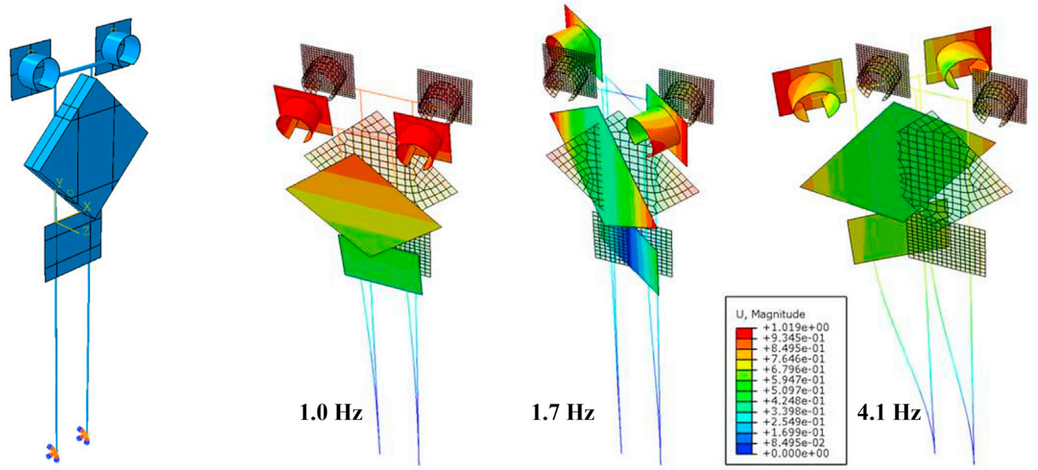

(**a**) RICWS geometry. (**b**) First three lowest eigenfrequencies and corresponding eigenmodes.

Fig. 14. Idealized RICWS configuration, discretization with beam/shell elements in Abaqus and eigenmode analysis.

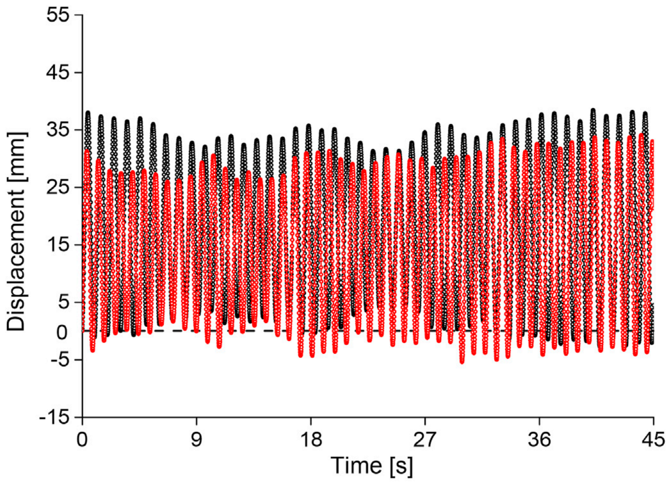

(**a**) Displacement history.

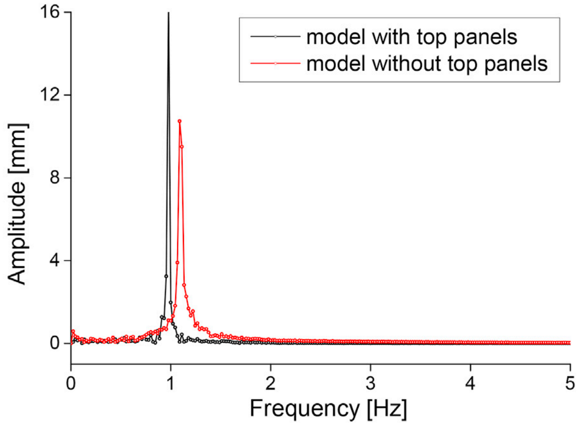

(**b**) Modal amplitudes.

Fig. 15. Dynamic response of the sign without top panels (in red), compared to the response of the original configuration (in black). (For interpretation of the references to colour in this figure legend, the reader is referred to the Web version of this article.)

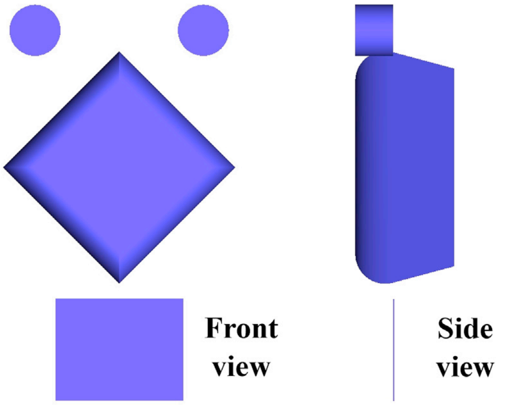

Fig. 16. Rear extensions at the main diamond-shaped panel.

“signature” turbulence generated by each configuration (known as “buffeting”). Both sources of turbulence are represented in the CFD simulations. As a result, we expect that the fluctuations of the wind forces depend on the incoming turbulence as well as the signature turbulence of each configuration of the sign structure. The aerodynamic action of the turbulence in a streamwise direction is often referred to as aerodynamic admittance (Jancauskas and Melbourne, 1986; Scanlan, 2000; Hejlesen et al., 2015), which relates the energy of the fluctuating forces to the energy of the fluctuations of the incoming velocity field with respect to the frequency. We conjecture that the insignificant reduction of the vibration response for modification 1 and the large reduction of the vibration response for modification 2, as illustrated in Table 5, can by explained by a comparison of the corresponding aerodynamic admittance to the one of the original configuration.

To underline this argument, we plot the power spectral densities (PSD) of the fluctuating force components for each sign configuration in Fig. 18. The PSD were estimated using Welch’s method with 20 s windows in every case (Welch, 1967). We made sure that the choice of window size did not affect the conclusions. In Fig. 18, we can observe that the sampled amplitudes are the same for the original configuration and the modification 1. For modification 2, however, the amplitude modulation with respect to frequency differs significantly from the one of the original configuration. We recall that the fluctuations of the flow

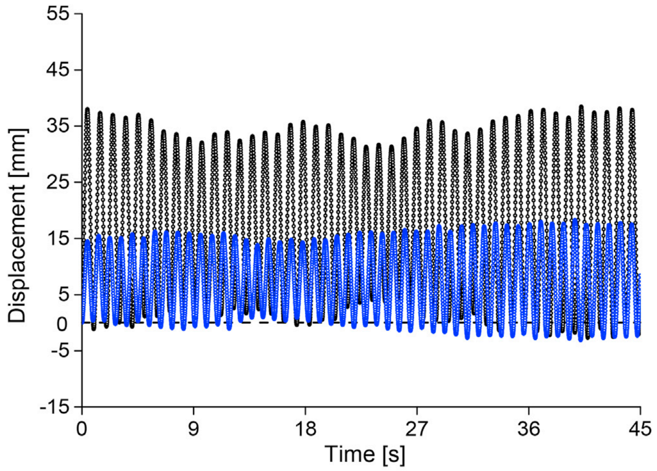

(a) Displacement history.

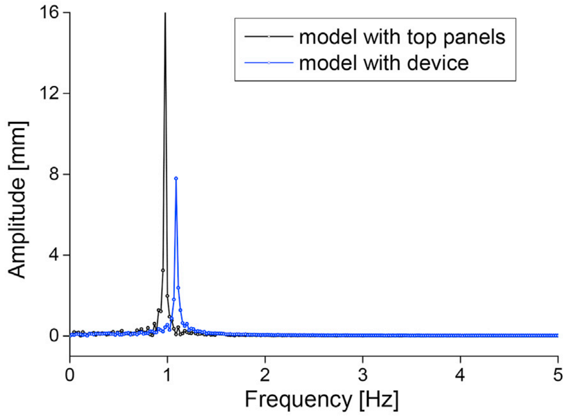

(b) Modal amplitudes.

Fig. 17. Dynamic response of the sign with drag reduction device (rear extension of diamond panel), compared to the response of the original configuration (in black).

Table 2
Drag force and drag coefficient for the original and modified RICWS configurations.

	Original RICWS structure	Modification 1 (top panels removed)	Modification 2 (rear extensions)
Mean drag force F_d	70.03 N (100%)	52.89 N (75%)	32.19 N (45%)
Standard dev. of F_d	2.68 N	2.54 N	2.60 N
Drag coefficient C_d	1.25	1.11	0.67

Table 3
Lift force and lift coefficient for the original and modified RICWS configurations. The negative sign indicates that the lift force acts downward.

	Original RICWS structure	Modification 1 (top panels removed)	Modification 2 (rear extensions)
Mean lift force F_l	−2.12 N (100%)	−1.02 N (48%)	−8.01 N (378%)
Standard dev. of F_l	0.51 N	0.58 N	1.22 N
Lift coefficient C_l	−0.24	−0.12	−0.35

Table 4
Pitching moment and moment coefficient for the original and modified RICWS configurations.

	Original RICWS structure	Modification 1 (top panels removed)	Modification 2 (rear extensions)
Mean moment M_{pitch}	227.06 Nm (100%)	168.80 Nm (74%)	101.86 Nm (45%)
Standard dev. of M_{pitch}	3.65 Nm	3.07 Nm	2.48 Nm
Moment coefficient C_M	1.13	0.99	0.60

Table 5
Vibration response in terms of critical eigenfrequency, mean deflection and averaged zero-mean peak-to-peak amplitude for the original and modified RICWS configurations.

	Original RICWS structure	Modification 1 (top panels removed)	Modification 2 (rear extensions)
Critical eigenfrequency	1.0 Hz	1.1 Hz	1.1 Hz
Mean deflection	17.81 mm (100%)	14.02 mm (79%)	7.51 mm (42%)
Peak-to-peak amplitude	41.15 mm (100%)	38.47 mm (93%)	21.37 mm (52%)

velocities upstream are equivalent for all three configurations, since we represent incoming turbulence with the same inflow boundary conditions (see Section 2.3) and the same parameters. We thus can conclude that the aerodynamic admittance of modification 1 is very similar to the one of the original configuration, and their vibration response will be similar as well. For modification 2, however, the vibration response is significantly reduced as a result of the change in aerodynamic admittance.

We emphasize that for the current simulations, the reduction in the vibration response is not connected to a resonance phenomenon. A resonance phenomenon is typically detected by a distinct peak in the associated power spectrum that can be still clearly seen when the amplitude distribution is plotted in logarithmic scale (see for instance (Païdoussis et al., 2010)). Some of the power spectra plotted in Fig. 18 show peaks, but they are comparatively small in comparison to the surrounding amplitudes and change location when the window size of the Welch transform is changed. We therefore conclude that at least the PSD peaks of the relevant force in streamwise direction are due to the restricted time history of 45 s and would smoothen out if a much longer time history was available. For modification 2, however, we could observe a consistent peak in its PSDs that occurs around 4 Hz. Its amplitude, however, remains relatively small and does not grow during the 45 s. We therefore assume that this phenomenon stays limited and is taken care of by structural damping.

From a theoretical viewpoint, our observations are in line with basic aeroelasticity (Païdoussis et al., 2010) that shows for much simpler configurations such as a cylinder that vortex shedding and its associated critical frequencies do not excite the response of the structure in streamwise direction, but the crosswind response at the shedding frequency. The maximum response occurs if the shedding frequency matches the natural frequency of the structure in the crosswind direction. For all sign configurations, however, the structure is much stiffer in the crosswind direction, such that the associated natural frequencies are much higher than the possible shedding frequencies, at least at practicable wind speeds.

5. Summary, conclusions and outlook

In this article, we first presented a CFD framework that combines the finite element method for the discretization of the incompressible Navier-Stokes equations, a subgrid-scale turbulence model based on the variational multiscale method, a synthetic eddy method for modeling incoming turbulence, and the FEniCS platform for high-performance computing. We then introduced the rural intersection conflict warning sign (RICWS) operated by the Minnesota Department of Transportation

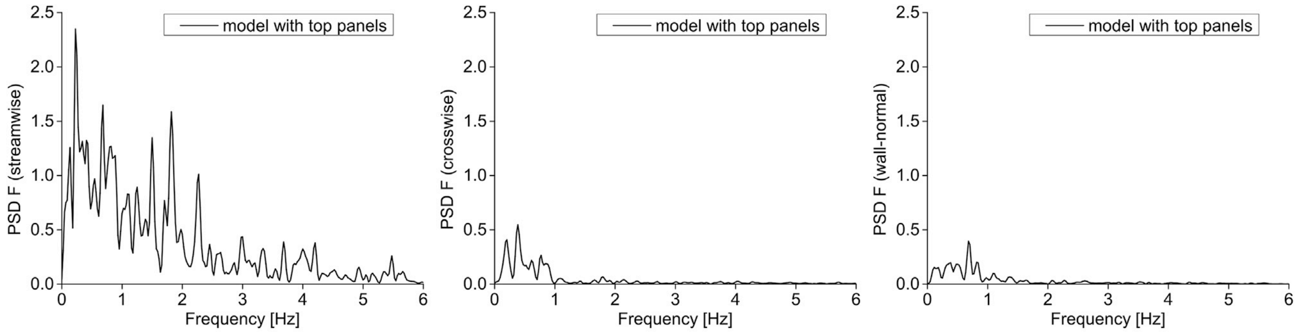

(a) Force in streamwise direction **(b)** Force in crosswise direction **(c)** Force in wall-normal direction

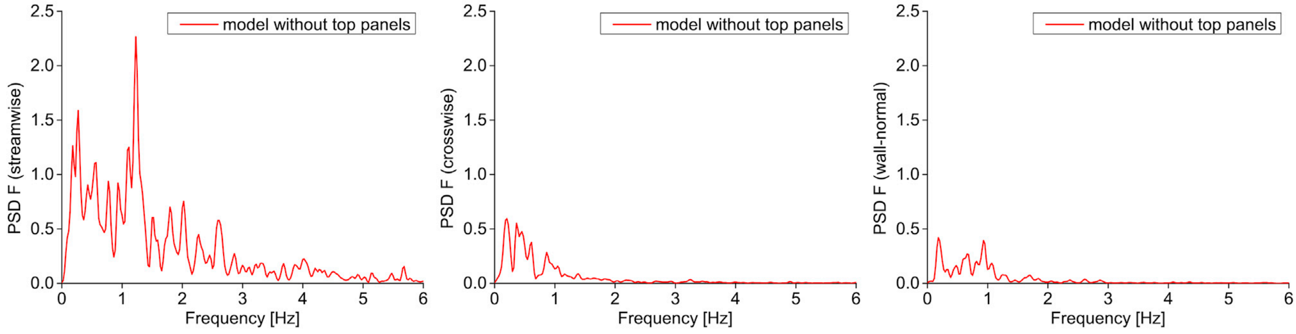

(d) Force in streamwise direction **(e)** Force in crosswise direction **(f)** Force in wall-normal direction

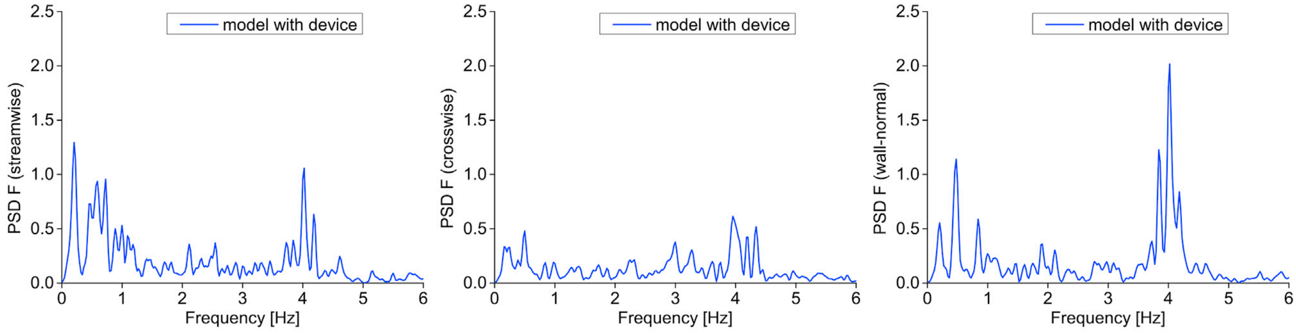

(g) Force in streamwise direction **(h)** Force in crosswise direction **(i)** Force in wall-normal direction

Fig. 18. Comparison of the PSD of the force in different directions for the three configurations.

as a representative example. Using experimental data obtained with a scaled RICWS model in the towing tank and the wind tunnel at the St. Anthony Falls Laboratory, we successfully validated our CFD framework at the lab scale.

Scaling our validated CFD model from the laboratory to the field scale, we computed the aerodynamic response of the original RICWS structure. Using the simulated pressure data as the transient loading input for a computational structural dynamics model in Abaqus, we obtained the reference vibration response for the case of head wind at the chosen wind speed. We then discussed two potential modifications of the original RICWS configuration, one based on the removal of the two top panels at the flashlights and one based on the addition of rear extensions behind the main diamond-shaped panel. Repeating the same computational procedure, we established the aerodynamic and structural response for each modified RICWS configuration. Due to a number of simplifying assumptions such as the exclusion of aeroelastic effects due to one-way coupling or the focus on the load case of head wind only, our results should be interpreted in a relative sense, having the main objective to enable comparison between the three configurations.

Our computational study enables the following key conclusions. First, our computational results reconfirm that modern CFD technologies constitute an effective and accurate tool for aerodynamic analysis of roadway signs. Second, our study demonstrates that carefully chosen aerodynamic modifications of roadway signs have the potential to clearly improve their aerodynamic behavior, in particular with respect to effectively limiting wind-induced structural vibrations as a key design concern. Third, our simulation results indicate that two factors, i.e. aerodynamic drag reduction and aerodynamic admittance for drag, influence the vibration behavior of the sign structure in different ways. While reduction of mean deflection correlates directly with the reduction of mean drag, the peak-to-peak amplitude of the oscillations is influenced by both the mean drag and the aerodynamic admittance for drag. For an effective reduction, aerodynamic modifications need to both minimize drag and control aerodynamic admittance.

We would like to emphasize again that the aerodynamic modifications presented here are tailored to the RICWS geometry under head wind. While the highlighted aerodynamic and structural benefits do not necessarily persist for different wind directions, the results provide a proof of concept that aerodynamic designs can be extended to road sign structures. Since aerodynamic modifications lead to a more streamlined design whose drag forces are Reynolds number dependent, one can anticipate a further reduction of the drag coefficient at higher design wind speeds.

The results of our computational study open up a number of avenues for future work. One direction is the further optimization of the shape and geometric parameters of rear extensions for different classes of road sign structures. Another direction is the further experimental and computational exploration of the corresponding aerodynamic and vibration response under different wind conditions and directions. For a competitive aerodynamic design, one needs to demonstrate favorable behavior for all wind directions. For example, the current design with rear extensions behaves very favorably under head wind, but is likely to increase drag under crosswind, since the added flaps increase the crosswind area. Finally, to further explore the coupled air-structure response for extreme wind speeds, the computational framework needs to be extended to fully nonlinear fluid-structure interaction and large structural deformations, see e.g. (Hsu and Bazilevs, 2012; Bazilevs et al., 2013).

Declaration of competing interest

The authors declare that they have no known competing financial interests or personal relationships that could have appeared to influence the work reported in this paper.

CRediT authorship contribution statement

Qiming Zhu: Methodology, Software, Validation, Formal analysis, Investigation, Data curation, Visualization. **Stein K.F. Stoter:** Methodology, Investigation, Writing - original draft. **Michael Heisel:** Validation, Writing - review & editing. **Catherine E. French:** Conceptualization, Funding acquisition. **Michele Guala:** Conceptualization, Methodology, Writing - review & editing, Supervision, Funding acquisition. **Lauren E. Linderman:** Conceptualization, Funding acquisition. **Dominik Schillinger:** Conceptualization, Methodology, Investigation, Writing - original draft, Supervision, Funding acquisition.

Acknowledgments

The authors gratefully acknowledge support from the Minnesota Department of Transportation via the project “Understanding and mitigating the dynamic behavior of RICWS and DMS under wind loading” within the Local Road Research Board program (grant no. 1003325, PI: L. Linderman). D. Schillinger gratefully acknowledges support from the National Science Foundation via the NSF CAREER Award No. 1651577. The authors also acknowledge the Minnesota Supercomputing Institute (MSI) of the University of Minnesota for providing computing resources that have contributed to the research results reported within this paper (https://www.msi.umn.edu/).

References

American Association of State Highway and Transportation Officials, 2015. Standard Specifications for Structural Supports for Highway Signs, Luminaires and Traffic Signals. AASHTO, Washington DC.
Ansys Inc, 2015. ICEM CFD Theory Guide.
Balakumar, B., Adrian, R., 2007. Large– and very–large–scale motions in channel and boundary–layer flows. Phil. Trans. Math. Phys. Eng. Sci. 365 (1852), 665–681.
Bazilevs, Y., Calo, V., Cottrell, J.A., Hughes, T., Reali, A., Scovazzi, G., 2007. Variational multiscale residual-based turbulence modeling for large eddy simulation of incompressible flows. Comput. Methods Appl. Mech. Eng. 197, 173–201.
Bazilevs, Y., Takizawa, K., Tezduyar, T., 2013. Computational Fluid-Structure Interaction: Methods and Applications. John Wiley & Sons.
Beneberu, E., Goode, J., Yazdani, N., 2014. Computational fluid dynamics application for design of highway sign support structures. Int. J. Civ. Struct. Eng. 5 (2), 101.
Brezzi, F., Franca, L., Hughes, T., Russo, A., 1997. $b=\int g$, computer methods in applied mechanics and engineering, 145, 329–339.
Browand, F., Radovich, C., Boivin, M., 2005. Fuel Savings by Means of Flaps Attached to the Base of a Trailer: Field Test Results. Tech. rep.. SAE Technical Paper.
Colomés, O., Badia, S., Codina, R., Principe, J., 2015. Assessment of variational multiscale models for the large eddy simulation of turbulent incompressible flows. Comput. Methods Appl. Mech. Eng. 285, 32–63.
Constantinescu, G., Bhatti, A., Tokyay, T., 2007. Improved Method for Determining Wind Loads on Highway Sign and Traffic-Signal Structures. Tech. rep., IHRB Project TR-559. Iowa Department of Transportation.
Constantinescu, G., Bhatti, A., Phares, B., 2018. Effect of Wind Induced Unsteady Vortex Shedding, Diurnal Temperature Changes, and Transit Conditions on Truss Structures Supporting Large Highway Signs. Tech. rep., IHRB Project TR-687. Iowa Department of Transportation.
Cummings, R., Mason, W., Morton, S., McDaniel, D., 2015. Applied Computational Aerodynamics: A Modern Engineering Approach, vol. 53. Cambridge University Press.
Dassault Systèmes, 2013. Abaqus Analysis User’s Manual (v6.13). Dassault Systèmes.
Davidson, L., Billson, M., 2006. Hybrid LES-RANS using synthesized turbulent fluctuations for forcing in the interface region. Int. J. Heat Fluid Flow 27 (6), 1028–1042.
Di Mare, L., Klein, M., Jones, W., Janicka, J., 2006. Synthetic turbulence inflow conditions for large-eddy simulation. Phys. Fluids 18 (2), 025107.
Donea, J., Huerta, A., 2003. Finite Element Methods for Flow Problems. Wiley.
Finley, N., 2018. Understanding and Mitigating the Dynamic Behavior of RICWS and DMS under Wind Loading. Master’s thesis. University of Minnesota.
Guala, M., Hommema, S., Adrian, R., 2006. Large-scale and very-large-scale motions in turbulent pipe flow. J. Fluid Mech. 554, 521–542.
Guala, M., Metzger, M., McKeon, B., 2011. Interactions within the turbulent boundary layer at high Reynolds number. J. Fluid Mech. 666, 573–604.
Håkansson, C., Lenngren, M.J., 2010. CFD Analysis of Aerodynamic Trailer Devices for Drag Reduction of Heavy Duty Trucks. Chalmers University of Technology.
Hejlesen, M., Rasmussen, J., Larsen, A., Walther, J., 2015. On estimating the aerodynamic admittance of bridge sections by a mesh–free vortex method. J. Wind Eng. Ind. Aerod. 146, 117–127.
Howard, K., Chamorro, L., Guala, M., 2016. A comparative analysis on the response of a wind-turbine model to atmospheric and terrain effects. Boundary-Layer Meteorol. 158 (2), 229–255.
Hsu, M., Bazilevs, Y., 2012. Fluid-structure interaction modeling of wind turbines: simulating the full machine. Comput. Mech. 50 (6), 821–833.
Hughes, T., 1995. Multiscale phenomena: Green’s functions, the Dirichlet–to–Neumann formulation, subgrid scale models, bubbles and the origins of stabilized methods. Comput. Methods Appl. Mech. Eng. 127 (1–4), 387–401.
Hughes, T., 2000. The Finite Element Method: Linear Static and Dynamic Finite Element Analysis. Dover Publications.
Hughes, T., Sangalli, G., 2007. Variational multiscale analysis: the fine-scale Green’s function, projection, optimization, localization, and stabilized methods. SIAM J. Numer. Anal. 45 (2), 539–557.
Hughes, T., Feijóo, G., Mazzei, L., Quincy, J.-B., 1998. The variational multiscale method – a paradigm for computational mechanics. Comput. Methods Appl. Mech. Eng. 166 (1), 3–24.
Hughes, T., Mazzei, L., Jansen, K., 2000. Large eddy simulation and the variational multiscale method. Comput. Visual Sci. 3 (1–2), 47–59.
Hughes, T., Calo, V., Scovazzi, G., 2005. Variational and multiscale methods in turbulence. In: Mechanics of the 21st Century. Springer, pp. 153–163.
Hughes, T., Scovazzi, G., Franca, L., 2018. Multiscale and Stabilized Methods. Encyclopedia of Computational Mechanics.
Hyams, D.G., Sreenivas, K., Pankajakshan, R., Nichols, D.S., Briley, W.R., Whitfield, D.L., 2011. Computational simulation of model and full scale class 8 trucks with drag reduction devices. Comput. Fluid 41 (1), 27–40.
Jancauskas, E., Melbourne, W., 1986. The aerodynamic admittance of two-dimensional rectangular section cylinders in smooth flow. J. Wind Eng. Ind. Aerod. 23, 395–408.
Jansen, K.E., Whiting, C.H., Hulbert, G.M., 2000. A generalized-α method for integrating the filtered Navier–Stokes equations with a stabilized finite element method. Comput. Methods Appl. Mech. Eng. 190 (3–4), 305–319.
Jarrin, N., Prosser, R., Uribe, J.-C., Benhamadouche, S., Laurence, D., 2009. Reconstruction of turbulent fluctuations for hybrid RANS/LES simulations using a synthetic-eddy method. Int. J. Heat Fluid Flow 30 (3), 435–442.
Logg, A., Mardal, K.-A., Wells, G., 2012. Automated Solution of Differential Equations by the Finite Element Method: the FEniCS Book, vol. 84. Springer Science & Business Media.
Lottes, S., Kulak, R., Bojanowski, C., 2011. Computational Mechanics Research and Support for Aerodynamics and Hydraulics at TFHRC. Tech. rep.. Argonne National Lab, Argonne, IL.
McCallen, R., Salari, K., Ortega, J., Castellucci, P., Paschkewitz, J., Eastwood, C., Dechant, L., Hassan, B., Pointer, W.D., Browand, F., et al., 2005. DOE’s Effort to Reduce Truck Aerodynamic Drag through Joint Experiments and Computations. Tech. rep.. SAE Technical Paper.
McGee, H., 2010. Maintenance of Signs and Sign Supports: A Guide for Local Highway and Street Maintenance Personnel. FHWA, Washington, DC.
F. Menter, Turbulence Modeling for Engineering Flows, Technical Paper (Ansys Inc.).
Oberkampf, W., Trucano, T., Hirsch, C., 2004. Verification, validation, and predictive capability in computational engineering and physics. Appl. Mech. Rev. 57 (5), 345–384.
Païdoussis, M., Price, S., De Langre, E., 2010. Fluid–structure Interactions: Crossflow–Induced Instabilities. Cambridge University Press.
Sagaut, P., 2006. Large Eddy Simulation for Incompressible Flows: an Introduction. Springer Science & Business Media.
Scanlan, R., 2000. Bridge deck aeroelastic admittance revisited. J. Bridge Eng. 5 (1), 1–7.
Schlichting, H., Gersten, K., 2016. Boundary-layer Theory. Springer.

Simiu, E., 2011. Design of Buildings for Wind: A Guide for ASCE 7–10 Standard Users and Designers of Special Structures. John Wiley & Sons.

Spalart, P., 2000. Strategies for turbulence modelling and simulations. Int. J. Heat Fluid Flow 21 (3), 252–263.

Storms, B., Satran, D., Heineck, J., Walker, S., 2004. A study of Reynolds number effects and drag-reduction concepts on a generic tractor-trailer. In: 34th AIAA Fluid Dynamics Conference and Exhibit, p. 2251.

Tezduyar, T., 1991. Stabilized finite element formulations for incompressible flow computations 28, 1–44.

Tezduyar, T., Osawa, Y., 2000. Finite element stabilization parameters computed from element matrices and vectors. Comput. Methods Appl. Mech. Eng. 28, 411–430.

Tran, S., Sahni, O., 2017. Finite element-based large eddy simulation using a combination of the variational multiscale method and the dynamic Smagorinsky model. J. Turbul. 18 (5), 391–417.

Welch, P., 1967. The use of fast Fourier transform for the estimation of power spectra: a method based on time averaging over short, modified periodograms. IEEE Trans. Audio Electroacoust. 15 (2), 70–73.

Wilson, E., 2010. Three-dimensional Static and Dynamic Analysis of Structures. Computers and Structures Inc., Berkeley, CA.

Witherden, F., Jameson, A., 2017. Aerodynamics. John Wiley & Sons, Ltd.

Yan, J., Korobenko, A., Tejada-Martínez, A., Golshan, R., Bazilevs, Y., 2017. A new variational multiscale formulation for stratified incompressible turbulent flows. Comput. Fluid 158, 150–156.

Yang, U.M., et al., 2002. BoomerAMG: a parallel algebraic multigrid solver and preconditioner. Appl. Numer. Math. 41 (1), 155–177.

Zienkiewicz, O., Taylor, R., 2005. The Finite Element Method – Fluid Dynamics, sixth ed., vol. 3. Butterworth-Heinemann.